

A Method for Combined Passive–Active Microwave Retrievals of Cloud and Precipitation Profiles

WILLIAM S. OLSON

Caelum Research Corporation, Silver Spring, Maryland

CHRISTIAN D. KUMMEROW AND GERALD M. HEYMSFIELD

NASA/Goddard Space Flight Center, Greenbelt, Maryland

LOUIS GIGLIO

Science Systems and Applications, Inc., Lanham, Maryland

(Manuscript received 2 February 1995, in final form 27 January 1996)

ABSTRACT

Three-dimensional tropical squall-line simulations from the Goddard cumulus ensemble (GCE) model are used as input to radiative computations of upwelling microwave brightness temperatures and radar reflectivities at selected microwave sensor frequencies. These cloud/radiative calculations form the basis of a physical cloud/precipitation profile retrieval method that yields estimates of the expected values of the hydrometeor water contents. Application of the retrieval method to simulated nadir-view observations of the aircraft-borne Advanced Microwave Precipitation Radiometer (AMPR) and NASA ER-2 Doppler radar (EDOP) produce random errors of 23%, 19%, and 53% in instantaneous estimates of integrated precipitating liquid, integrated precipitating ice, and surface rain rate, respectively.

On 5 October 1993, during the Convection and Atmospheric Moisture Experiment (CAMEX), the AMPR and EDOP were used to observe convective systems in the vicinity of the Florida peninsula. Although the AMPR data alone could be used to retrieve cloud and precipitation vertical profiles over the ocean, retrievals of high-resolution vertical precipitation structure and profile information over land required the combination of AMPR and EDOP observations.

No validation data are available for this study; however, the retrieved precipitation distributions from the convective systems are compatible with limited radar climatologies of such systems, as well as being radiometrically consistent with both the AMPR and EDOP observations. In the future, the retrieval method will be adapted to the passive and active microwave measurements from the Tropical Rainfall Measuring Mission (TRMM) satellite sensors.

1. Introduction

Recent climate modeling studies have shown the importance of three-dimensional atmospheric heating distributions in the forcing of large-scale circulations in the Tropics (Hartmann et al. 1984; DeMaria 1985; Lau and Peng 1987). These large-scale circulations are intimately linked to climate variations in the Tropics, as well as observed changes in weather regimes at higher latitudes (Trenberth et al. 1988). The latent heating associated with precipitation, however, has not been independently observed over the large space and time scales needed for climate analyses and the validation of general circulation model simulations.

The combination of satellite-borne passive and active sensors to be deployed in the upcoming Tropical Rainfall Measuring Mission (TRMM) promises to provide critical information regarding the three-dimensional distributions of precipitation and heating in the Tropics (Simpson et al. 1988). Chief among the TRMM sensors are the TRMM Microwave Imager and the Precipitation Radar. Both of these instruments operate at microwave frequencies, where electromagnetic radiation can penetrate to various depths in precipitating clouds. Since cloud heating and cooling distributions are related to the vertical profiles of cloud and precipitation water contents (Tao et al. 1993), measurements from these sensors should help to construct the desired heating analyses.

Coincident measurements from passive and active microwave sensors are complementary: passive microwave radiometers measure radiances that are the end product of the integrated effects of electromagnetic ab-

Corresponding author address: Dr. William S. Olson, NASA/GSFC, Code 912, Greenbelt, MD 20771.
E-mail: olson@audry.gsfc.nasa.gov

sorption/emission and scattering through a precipitating cloud along the sensor viewpath. The frequency dependence of electromagnetic properties of cloud and precipitation particles allows for the design of multi-channel passive microwave radiometers, which can "sound" to different depths in a precipitating cloud, but the height assignment of cloud properties is not very specific. On the other hand, active microwave sensors (radars) provide specific height information based upon the time delay of the precipitation-backscattered return power. However, simple one-parameter radars (such as the TRMM Precipitation Radar) operate only at one transmitting-receiving frequency and polarization. To obtain unambiguous precipitation water content profiles from these radars, secondary signal effects such as path-integrated attenuation must be determined independently.

If, at a minimum, passive microwave measurements can provide path-integrated attenuation information, then the combination of passive and active microwave sensors should yield height-specific information regarding cloud and precipitation water contents. Still, the interpretation of data from the combined radiometer-radar system is complicated by other factors that have an impact on the measured signals. These factors include the precipitation particle size distributions, the phase of the hydrometeors (with possibly mixed-phase particles), the geometry of the precipitating cloud, the humidity of the cloud environment, and the state of the underlying earth's surface.

Although several authors have proposed physically based methods for retrieving precipitation profiles based upon passive microwave radiometer measurements (Olson 1989; Kummerow et al. 1989; Mugnai et al. 1993; Smith et al. 1994; Kummerow and Giglio 1994; Evans et al. 1995) or radar measurements (Hitschfeld and Bordan 1954; Meneghini 1978; Meneghini et al. 1983; Meneghini and Nakamura 1990; Kozu et al. 1991; Marzoug and Amayenc 1991), only a few have described methods that combine passive radiometer and radar data. Hai et al. (1985) inverted radar power measurements using the total path-extinction derived from coincident radiometer measurements at the same frequency as a constraint. With this method, they retrieved cloud liquid water distributions from ground-based Ka-band (35 GHz) radiometer-radar measurements, which were superior to estimates based upon radar measurements alone. Weinman et al. (1990) used X-band (10 GHz) radiometer derived path-integrated extinction to estimate the total attenuation of radar reflectivities at X band (10 GHz) and Ka band (34.45 GHz). Using the total path-integrated extinction as a boundary condition, these authors solved a form of the Hitschfeld-Bordan equation to obtain profiles of extinction from radar reflectivity measurements. Derived rain-rate profiles compared well with profiles determined from dual-wavelength radar. More recently Kumagai et al. (1993) used single-frequency

radar reflectivities to retrieve a profile of precipitation drop size distribution slopes, and then determined the common intercept of the size distributions from passive radiometer measurements. This methodology was extended by Meneghini et al. (1994) to retrieve profiles of two precipitation drop size distribution parameters from dual-frequency radar/total attenuation measurements for several humidity/cloud water environments. The proper precipitation profile and its humidity/cloud water environment were then selected by comparing radiative transfer computations of the upwelling brightness temperatures from each precipitation profile to observed brightness temperatures. Finally, Haddad and Im (1993) have proposed a method for estimating the probability density function of rain rate conditioned on measurements of radar reflectivity and radiometer-derived attenuation at each radar range gate. The method yields a profile of rain-rate probability density functions from which a profile of mean rain rates and associated error standard deviations can be obtained.

The primary motivation in the present work is to develop a computationally efficient physical retrieval methodology that can be utilized in conjunction with the data from the TRMM passive and active microwave sensors to estimate cloud and precipitation water content profiles. Since the TRMM Precipitation Radar has a relatively narrow swath that coincides with only 30% of the passive radiometer (TRMM Microwave Imager) swath, one additional design criterion is that the retrieval method framework should be applicable if either radiometer/radar data or only radiometer data are available.

In the present study, fully three-dimensional cloud model simulations are used as input to radiative computations of both upwelling brightness temperatures and radar reflectivities at selected microwave sensor frequencies. These cloud/radiative calculations form the basis of a cloud/precipitation profile retrieval method that yields estimates of the expected values of the cloud and precipitation water contents. Application of this method is computationally much less intensive than the commonly used iterative minimum variance method, and it is easily expanded to include not only passive and active microwave channels, but also infrared and other sensor data as well as available a priori information.

The retrieval method is applied to the aircraft-borne Advanced Microwave Precipitation Radiometer (AMPR) and combined AMPR-ER-2 Doppler radar system (EDOP) data from the Convection and Atmospheric Moisture Experiment (CAMEX). The basic specifications of these instruments are listed in Table 1, along with the specifications of the TRMM Microwave Imager and Precipitation Radar for comparison.

From Table 1 it may be noted that the AMPR channels cover a range of microwave frequencies from 10.7 to 85.5 GHz. The radiative properties of clouds and precipitation vary significantly over this range. Over a

TABLE 1. Basic specifications of the Advanced Microwave Precipitation Radiometer, NASA ER-2 Doppler radar, TRMM Microwave Imager, and Precipitation Radar. AMPR specifications are from Spencer et al. (1994). The horizontal resolution specifications of the AMPR, EDOP, and Precipitation Radar are at nadir view.

Channel frequency (GHz)	Half-power beamwidth (°)	Horizontal resolution at surface (km)	Noise (K)
AMPR			
10.7	8.0	2.8	0.27
19.35	8.0	2.8	0.30
37.1	4.2	1.5	0.15
85.5	1.8	0.6	0.18
TRMM Microwave Imager			
10.65	3.95	38.3×63.2	0.93
19.35	1.9	18.4×30.4	1.02
21.3	1.7	16.5×27.5	1.18
37.0	1.0	9.7×16.0	0.74
85.5	0.45	4.4×7.2	1.10
Channel frequency (GHz)	Half-power beamwidth (°)	Horiz. resolution at surface/range resolution (km)	Uncertainty due to sampling (dB)
EDOP			
(during CAMEX)			
9.72	2.9	1.0/0.15	0.8
Precipitation Radar			
13.8	0.71	4.3/0.25	0.7

low-emissivity, water surface background at 10.7 GHz, the effect of a precipitation-free atmosphere on upwelling microwave brightness temperatures is minimal, while absorption and emission by liquid precipitation can raise the observed brightness temperature by as much as 100 K. The increase of brightness temperature with vertically integrated rainwater content is generally linear at this frequency. However, at a sufficiently high water content (near 13 kg m^{-2}) the rain column becomes so optically thick that the upwelling brightness temperature plateaus, or "saturates," at a value close to the physical temperature of the top of the rain column. Since absorption of microwaves by liquid cloud and rain increases with frequency, the water content for which the brightness temperature saturates decreases with frequency. At 19.35, 37.1, and 85.5 GHz, the brightness temperature first increases and then saturates near 6, 2, and 0.7 kg m^{-2} , respectively, over a water surface background. In addition to the effects of liquid cloud and rain scattering by ice-phase precipitation, which is almost negligible at 10.7 GHz, increases with frequency and becomes significant at 37.1 GHz and dominant at 85.5 GHz for ice precipitation columns greater than 1 kg m^{-2} . Scattering lowers the observed brightness temperature by diverting radiation from the upwelling radiance path. Large amounts of graupel and/or hail may be present in organized convective

systems, and scattering signatures of 150 K have been measured by AMPR at 85.5 GHz in convective storms over the ocean; see Spencer et al. (1994), Smith et al. (1994b), and Turk et al. (1994). Over land, microwave emission from liquid cloud and rain is difficult to distinguish from the more highly emissive land background. However, brightness temperature scattering depressions due to ice-phase precipitation are still detectable over land and often exceed those over ocean surfaces. The greater atmospheric instability over land leads to increased convective core updraft velocities and greater concentrations of ice-phase precipitation held aloft. Turk et al. (1994) report 85.5-GHz AMPR brightness temperatures less than 100 K in observations of convective cells over land.

For rain radar systems the effective reflectivity is roughly proportional to the square of the precipitation water content, with ice-phase precipitation being about 20% as reflective as liquid. However, both the EDOP and Precipitation Radar are relatively high frequency (short-wavelength) radars, and so the effective reflectivity can be significantly reduced due to attenuation by cloud and precipitation between the radar and the precipitation target. The EDOP operates at 9.72-GHz (3.1 cm) frequency, which is lower than the frequency of the TRMM Precipitation Radar (13.8 GHz; 2.2 cm). Therefore, EDOP is less affected by attenuation than the Precipitation Radar. Since both instruments are downward-looking, signal attenuation effects are most severe at the base of a liquid precipitation column. For example, a 4.5-km column of rain with a water content of 0.62 g m^{-3} (equivalent to a 10 mm h^{-1} rain rate) would attenuate the EDOP signal by 1.6 dB, while the Precipitation Radar would suffer a 3.7-dB loss.

Although the airborne AMPR and EDOP operate at nearly the same frequencies as the TRMM Microwave Imager and Precipitation Radar, the horizontal resolution of the airborne sensors is much higher than the horizontal resolution of the TRMM satellite instruments. The airborne AMPR and EDOP have a surface resolution of about 1 km, which is adequate for resolving most precipitation structures, while the TRMM sensors would average the signals from adjacent convective elements. Because there is greater averaging of precipitation signals in the lower-resolution satellite measurements, the relationships between precipitation water contents and the satellite measurements are more ambiguous, and precipitation retrievals from these data are more difficult. In the present study, precipitation profile retrievals based upon the higher-resolution airborne sensor measurements are examined in an attempt to evaluate retrieval performance in the absence of complicating signal-averaging effects. Applications of the retrieval method to simulated TRMM Microwave Imager and Precipitation Radar measurements will be the subject of a future investigation by the authors.

2. Retrieval method

A schematic of the profile retrieval method is shown in Fig. 1. Prior to the application of the method a large database of cloud/precipitation profiles is generated using a numerical cloud model, and the passive microwave radiometric brightness temperatures and active microwave (radar) reflectivities associated with each model profile are calculated based upon radiative transfer theory. In the retrieval procedure, the brightness temperatures and radar reflectivities from each model profile together with the observed brightness temperatures and reflectivities are used to compute the probability that the model profile is indeed the observed profile. The model profiles are weighted by their respective probabilities and summed to create a composite best estimate of the observed profile. In the subsections that follow the creation of the cloud/radiative model database and theoretical basis for the retrieval method are described in detail.

a. The cloud model

The cloud model utilized in this study is originally based upon the cloud ensemble model of Tao and Soong (1986). However, several improvements have been made over the last decade at NASA/Goddard Space Flight Center, and the model was officially renamed the Goddard cumulus ensemble (GCE) model in 1989. A detailed description of the current GCE model formulation may be found in Tao and Simpson (1993).

The GCE model is a nonhydrostatic and anelastic numerical cloud model, and so in addition to the basic prognostic equations, conservation equations for two liquid water species (cloud and raindrops), and three ice-phase species (cloud ice, snow, and graupel) are included in the formulation. Liquid water microphysics are represented using a Kessler-type scheme, and ice-phase processes are based upon the formulations of Lin et al. (1983) and Rutledge and Hobbs (1984). Cloud liquid and cloud ice particles are assumed to be monodisperse, 20- μm -diameter spheres, while rain, snow, and graupel are assumed to be spherical and have inverse exponential size distributions of the form

$$n(D) = n_0 \exp(-\alpha D), \quad (1)$$

where D is the particle diameter, and n_0 is set equal to either 0.08 cm^{-4} for rain, as in the Marshall and Palmer (1948) size distribution, or 0.04 cm^{-4} for snow and graupel, as in Rutledge and Hobbs (1984). The variable α has a value

$$\alpha = \left(\frac{\pi \rho_i n_0}{M_i} \right)^{1/4}. \quad (2)$$

This formula for α is required for the integral over all hydrometeor diameters of the mass density of hydrometeors to equal the modeled liquid water content, M_i .

Retrieval Method

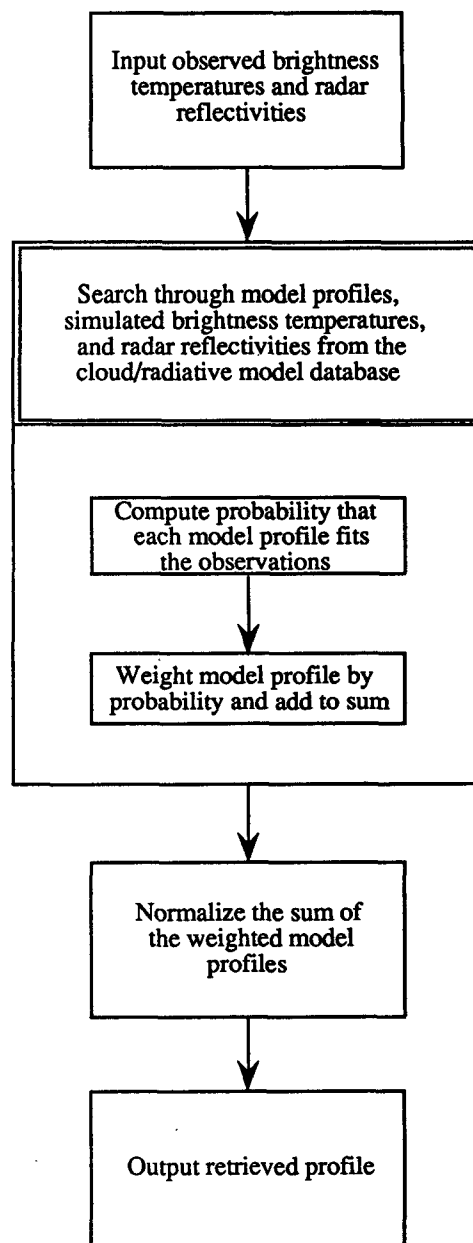


FIG. 1. Flow diagram for the combined passive-active microwave precipitation profile retrieval method.

Here, ρ_i is the mass density of water substance within each hydrometeor of species i . Rain has a mass density equal to 1.0 g cm^{-3} , while snow and graupel are assumed to have densities of 0.1 and 0.4 g cm^{-3} , respectively.

Other features of the GCE model include a parameterization for the effects of short- and longwave radiation, a representation of subgrid-scale turbulent mix-

ing processes through a turbulent kinetic energy equation, and a parameterization of heat and moisture fluxes from an underlying ocean surface (when applicable).

The GCE model uses a stretched vertical coordinate with height increments ranging from 220 to 1050 m (31 grid points) to maximize resolution at the lowest levels. Current computer limits restrict the horizontal model domain to a 128×128 grid at 1- or 1.5-km resolution, and periodic or open boundary conditions may be imposed. A Galilean transformation of the model base-state wind field is used to keep a propagating cloud system near the center of the domain.

Two different tropical squall-line simulations performed using the GCE model are utilized in the present study. The first was initialized using a composite of atmospheric soundings taken during the GARP Atlantic Tropical Experiment (GATE); see Barnes and Sieckman (1984). Also a domain-wide, time-dependent vertical velocity field derived from radiosonde data by Ogura et al. (1979) was imposed on the model to simulate the effects of observed larger-scale lifting on the development of convection. The GCE model GATE simulation was performed on a 64×64 , 1.5-km resolution grid domain, with periodic boundary conditions in the horizontal. Surface fluxes were omitted from this simulation.

Many of the modeled squall-line features are consistent with GATE observations. The explosive growth of the convex leading edge, the orientation of the convective line perpendicular to the environmental wind shear, and the propagation speed of the squall system are all in agreement with observations. However, some features of the simulated squall line are at a variance with observations. The imposed domain-wide lifting profiles led to excessive destabilization of the atmosphere, which, in combination with an unmodified Rutledge and Hobbs (1984) microphysics scheme caused unrealistically large amounts of graupel to be produced in some convective cells. Also, aspects of the stratiform precipitation region, such as the proportion of stratiform rainfall and its fractional coverage, were not adequately reproduced because of the limited model domain ($96 \text{ km} \times 96 \text{ km}$) and short model integration period (240 min). A detailed description of the GATE squall-line simulation may be found in Tao and Simpson (1989); it is referenced as the 3D simulation, which includes ice microphysical processes.

The second tropical squall-line simulation was initialized using an environment observed during the Tropical Ocean Global Atmosphere Coupled Ocean–Atmosphere Response Experiment (TOGA COARE). The initial vertical profiles of temperature, humidity, and horizontal winds were derived from NOAA P-3 aircraft flight level data and rawinsonde observations of the environment in immediate advance of the 22 February 1993 squall line as described by Trier et al. (1994). In the TOGA COARE simulations, the advection scheme of Smolarkiewicz (1983, 1984) with a

nonoscillatory option (Smolarkiewicz and Grabowski 1990) was incorporated into the GCE model. In contrast to the GATE simulation, no lifting profile was imposed on the modeled cloud environment. The model domain was increased to 128×128 at 1-km resolution, and the domain boundaries were assumed to be open in the X direction (the direction of storm propagation) and periodic in the Y direction. Surface fluxes of momentum, heat, and moisture were included using bulk aerodynamic formulas.

In the TOGA COARE simulation the GCE model produces a squall line with upshear-tilted convection and a significant stratiform region that yields more than 50% of the total storm rainfall in the mature stage of development. Although the $128 \text{ km} \times 128 \text{ km}$ model domain limits the horizontal extent of the model squall line, the structure of the simulated precipitation distribution compares reasonably well with NOAA P-3 radar observations of the most active portion of the mature 22 February 1993 TOGA COARE squall line (see Fig. 4 of Jorgensen et al. 1994; Fig. 1b of Jorgensen et al. 1995). The eastern boundary of the simulated storm is marked by a bowed convective leading edge with arms extending to the northwest and southwest, and a mixture of convective and stratiform precipitation to the west of the convective boundary. Stratiform precipitation predominates to the west of the northernwestern arm of the storm. Upshear-tilted convection and a bowed leading edge were also seen in P-3 radar observations of the actual squall line. The observed leading edge convection extended to the northwest and south, although the southern branch was oriented more east–west than in the simulated storm. Mixed convective and stratiform precipitation trailed the leading edge of the storm to the west.

The three-dimensional cloud and precipitation structures simulated at five different times (126, 138, 174, 210, and 234 min) in the GATE model run and at eight different times (30, 60, 90, 120, 150, 180, 210, and 240 min) in the TOGA COARE model run are utilized as input to the radiative computations described in the next subsection.

b. Radiative transfer calculations

1) UPWELLING BRIGHTNESS TEMPERATURES

Upwelling microwave radiances at the top of the atmosphere originate partly from the earth's surface and partly from atmospheric constituents. The emissivity of the earth's surface is determined by the frequency, incidence angle, and polarization of the radiation, and by the complex index of refraction of the surface as described by the Fresnel relations. Over water, the refractive index is a function of the water temperature, salinity, and foam coverage induced by wind driven waves. The model of Wilheit (1979) is used here to compute the water surface emissivity as a function of

near-surface wind speed. Over land, the surface emissivity is assumed to result primarily from dry soil, but with varying fractional coverage by standing water.

Among the atmospheric absorbers of microwave radiation, water vapor, molecular oxygen, and cloud water need to be considered. In this study, both the water vapor absorption as well as the oxygen absorption are calculated from Liebe (1985). Nonprecipitating cloud particles are of the order of 100 μm or less in diameter. This dimension is much smaller than typical microwave wavelengths, which range from 3 cm at 10 GHz to 3.5 mm at 85 GHz. As a result, the Rayleigh approximation is employed to calculate the absorption coefficient of cloud water. The larger, non-Rayleigh precipitation particles are assumed to be spherical, and so Mie theory is employed to calculate the extinction coefficient k_{ext} , single-scatter albedo ω_0 , phase function p , and asymmetry factor g of the precipitation particle distributions produced by the cloud model.

Microwave brightness temperatures at selected passive radiometer frequencies and viewing angles are calculated by repeated application of the one-dimensional version of Eddington's second approximation (Weinman and Davies 1978). In the present treatment, all radiance slant paths through the cloud model domain are considered independently.

Upwelling microwave brightness temperature computations at model resolution (~ 1 km) are performed for each of the 13 GCE model-simulated tropical squall-line cloud and precipitation fields. For each cloud model field, brightness temperatures are computed assuming four different water and land surface backgrounds. The backgrounds are varied in order to account for variations of the surface emissivity, which may be encountered in applications of the retrieval method described in section 2c. Over water, emissivities corresponding to 20-m wind speeds of 0, 6, 12, and 18 m s^{-1} are computed using the Wilheit (1979) model. Over land, different emissivities are computed by taking the areal-mean emissivity for water coverage fractions of 0, 0.043, 0.08, and 0.12. By superimposing the cloud model atmospheres over the different water and land surface backgrounds, a total of four nadir-view brightness temperatures for each atmospheric profile over both water and land are computed.

Examples of the computed microwave brightness temperatures from the GATE and TOGA COARE squall-line simulations are presented in Figs. 2a–c and 3a–c. Figure 2a is a plan view of the distribution of vertically integrated total precipitation (rain, snow, and graupel) from the GATE squall-line simulation at 210 min. Note the convex precipitation distribution with the most intense convection appearing near $X = 24$ km; $Y = 40$ and 68 km. Computed nadir-view brightness temperatures at 10.7 and 85.5 GHz associated with this model field are shown in Figs. 2b and 2c, respectively. At 10.7 GHz, the assumed calm water surface background has a low emissivity, and net upwelling bright-

ness temperatures are less than 140 K. The brightness temperature signal from precipitation is primarily due to absorption and reemission from rain, with maximum brightness temperatures greater than 260 K near the convective cores. In contrast, the higher water surface emissivity and enhanced emission from water vapor at 85.5 GHz result in "clear-air" brightness temperatures greater than 220 K. Regions of cloud and/or light rain produce brightness temperatures that can exceed 260 K at the periphery of the storm; however, heavier rain and snow/graupe scatter microwave radiances, and in the net brightness temperatures decrease as radiant energy is scattered out of the upwelling beam. Maximum scattering depressions less than 140 K are seen in the convective core regions, which can support ice hydrometeor growth with stronger updrafts.

Presented in Fig. 3a is a plan view of the simulated TOGA COARE total precipitation distribution at 180 min. The highest liquid precipitation amounts occur in the bow-shaped convective leading edge of the squall line, and liquid water emission at 10.7 GHz (Fig. 3b) exceeds 260 K along the leading edge. In contrast to the GATE simulation, updrafts in the leading edge are relatively weak, resulting in low ice precipitation concentrations and relatively high brightness temperatures at 85.5 GHz (Fig. 3c). Scattering signatures below 220 K are observed only in isolated pockets to the rear of the system along $X = 50$ km.

2) REFLECTIVITIES

In addition to the forward radiative model for computing upwelling microwave brightness temperatures, a model describing active radiometer (radar) response is also developed. The physics of radar response is embodied in the radar equation (Sauvageot 1992),

$$P_r = \frac{CZ_t}{r^2}, \quad (3)$$

where the power detected by the receiver is proportional to the total reflectivity Z_t of the atmospheric target, and is inversely proportional to the square of the range r of the target. Constant C depends upon the specifics of the radar configuration and the dielectric constant of liquid water.

The total reflectivity Z_t of the atmospheric target is represented by

$$Z_t = \frac{\lambda^4}{4\pi^6 |K_l|^2} \{ k_{\text{ext}}(r) \omega_0(r) p(r, 180^\circ) \} \\ \times \exp \left[-2 \int_0^r k_{\text{ext}}(s) ds \right] + Z_n. \quad (4)$$

Here, $|K_l|^2$ is a liquid water dielectric factor that has a value of 0.93, λ is the radar wavelength, and s is the distance measured along the slant path of the radar beam. The term in curly brackets is the backscatter

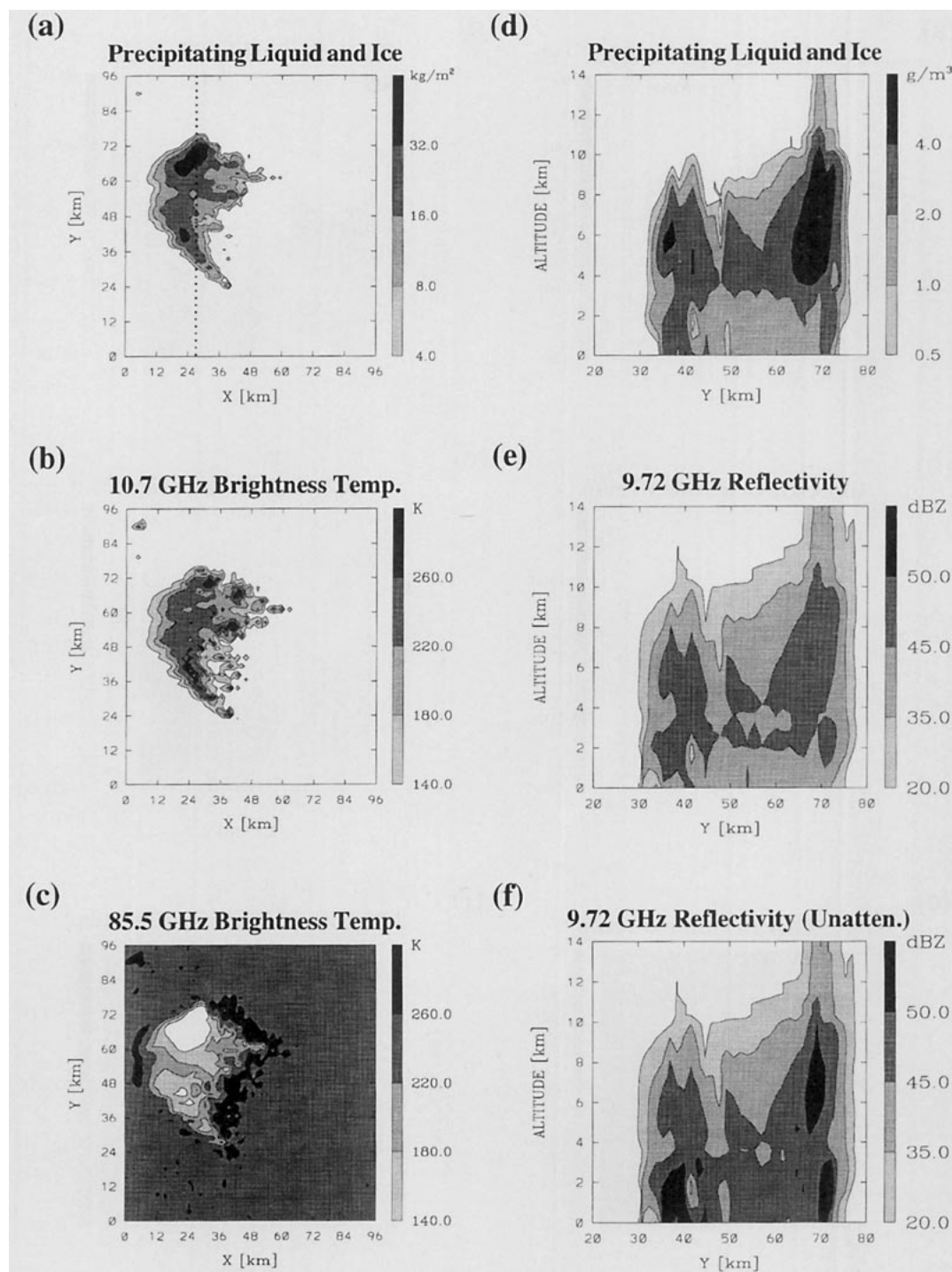


FIG. 2. Precipitation, brightness temperature, and radar reflectivity fields based upon the 210-min GATE GCE model simulation over a calm water surface. (a) A plan view of the vertically integrated total precipitation water content. (b) and (c) The associated nadir-view upwelling brightness temperatures computed at 10.7 and 85.5 GHz, respectively. (d) The vertical cross section of total precipitation water content at $X = 27$ km, between $Y = 20$ and 80 km. (e) and (f) The associated cross sections of path-attenuated and unattenuated radar reflectivities at 9.72 GHz.

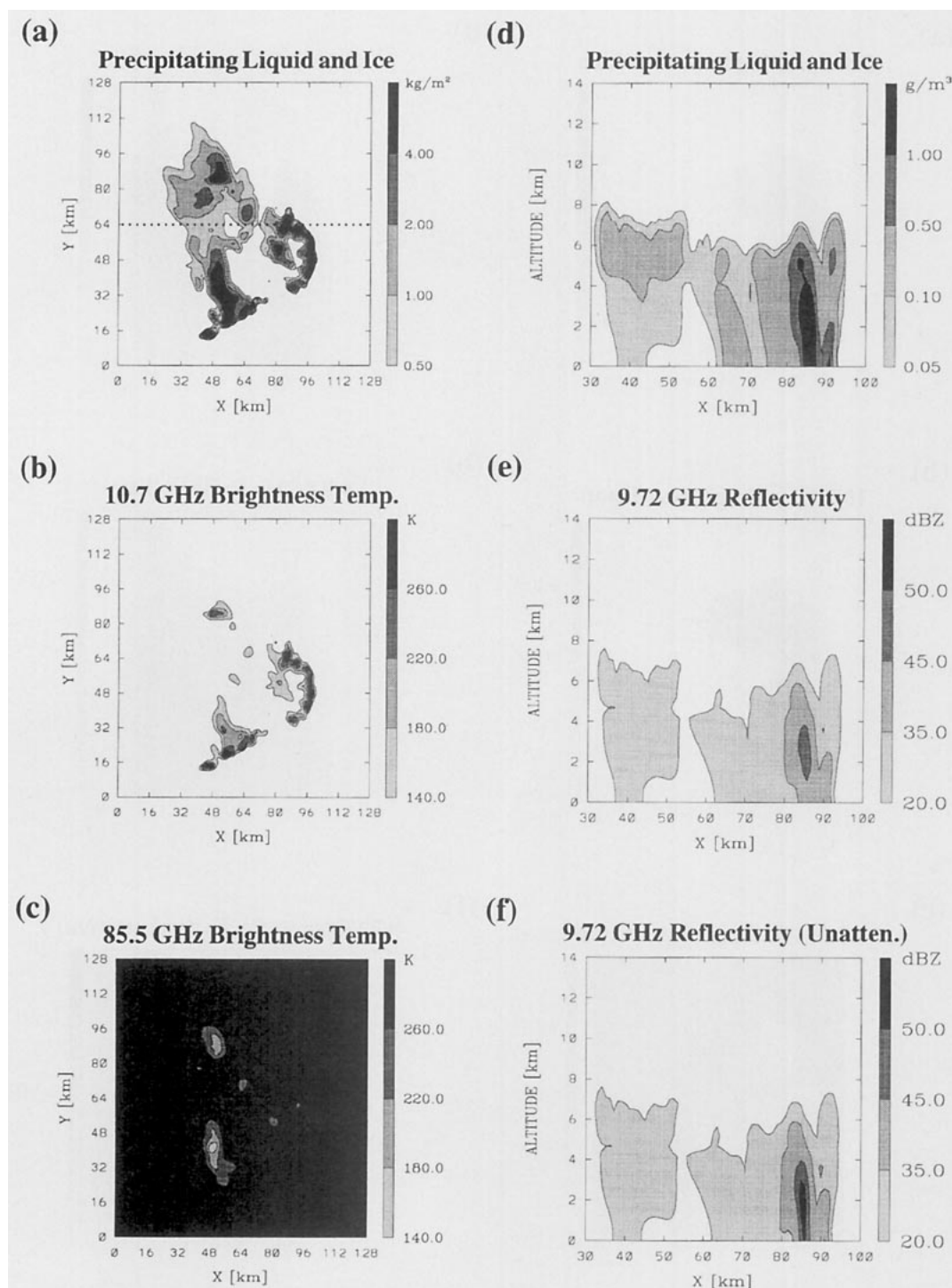


FIG. 3. Precipitation, brightness temperature, and radar reflectivity fields based upon the 180-min TOGA COARE GCE model simulation over a calm water surface. (a) A plan view of the vertically integrated total precipitation water content. (b) and (c) The associated nadir-view upwelling brightness temperatures computed at 10.7 and 85.5 GHz, respectively. (d) The vertical cross section of total precipitation water content at $Y = 64$ km, between $X = 30$ and 100 km. (e) and (f) The associated cross sections of nadir-view, path-attenuated, and unattenuated radar reflectivities at 9.72 GHz.

cross section of the atmospheric target, where $p(r, 180^\circ)$ is the backscatter phase function of the target at range r . The exponential term in Eq. (4) represents the two-way attenuation of the radar pulse from the transmitter to the target and back. Here, Z_n is the equivalent reflectivity of additional thermal noise power that contributes to the radar-measured total power,

$$Z_n = \frac{r^2 B T_{sy} \Delta f}{C}, \quad (5)$$

where B is the Boltzman constant ($1.38 \times 10^{-23} \text{ J K}^{-1}$), T_{sy} is the system temperature, and Δf is the receiver bandwidth. Not included in Eq. (4) are small contributions from multiply scattered pulse power received by the radar.

If the radar is carried aloft by an aircraft or satellite at an altitude z_a above an assumed plane-parallel atmosphere, then the reflectivity measurement of the atmospheric layer at altitude z is

$$Z_r = \frac{\lambda^4}{4\pi^6 |K_l|^2} \{ k_{\text{ext}}(z) \omega_0(z) p(z, 180^\circ) \} \\ \times \exp \left[-2 \int_z^{z_a} \frac{k_{\text{ext}}(z') dz'}{\cos \theta_0} \right] + Z_n, \quad (6)$$

where θ_0 is the incidence angle of the radar beam at the earth's surface. This reflectivity relationship is applicable to all atmospheric radar targets that do not involve surface reflection of the transmitted/received radar pulse. The applications in this study will not include these latter targets.

As in the case of the brightness temperature forward model, the radiative parameters k_{ext} , ω_0 , and p are specified, based upon the prescribed pressure, temperature, humidity, and the water contents of the various cloud species (cloud water, rain, cloud ice, snow, and graupel) at each level in the cloud model atmosphere. Radar reflectivities at cloud model resolution (approximately 1 km in the horizontal and vertical) are computed for each of the 13 selected GCE model-simulated cloud and precipitation fields.

Cloud model vertical precipitation structures and computed radar reflectivity profiles from the GATE and TOGA COARE simulations are presented in Figs. 2d–f and 3d–f, respectively. In Fig. 2d, a vertical cross section of total precipitation water content (rain, snow, and graupel) from the modeled GATE squall line at 210 min; $X = 27$ km is shown. The corresponding path-attenuated reflectivities for a nadir-viewing radar operating at 9.72 GHz are presented in Fig. 2e. Note that the maximum radar reflectivities (greater than 45 dBZ) are located in the convective core regions at altitudes greater than 2 km. The effects of path-integrated attenuation are revealed by comparing Fig. 2e to the “unattenuated” reflectivities for the same precipitation distribution in Fig. 2f. The highly reflective (>50 dBZ) cores that extend down to the surface at $Y = 38$ and 72

km in Fig. 2f are obscured by overlying precipitation in the path-attenuated reflectivity profiles.

The vertical cross section of total precipitation water content from the modeled TOGA COARE squall line at 180 min; $Y = 64$ km is shown in Fig. 3d. Associated with the leading edge convection, precipitation water contents greater than 1 g m^{-3} extend from the surface to about 5.5-km altitude. Although precipitation water contents are typically lower in the TOGA COARE simulation relative to the GATE simulation, significant attenuation of radar reflectivities in convective regions still occurs, as indicated by Figs. 3e and 3f.

3) ANTENNA PATTERN EFFECTS

The fields of simulated brightness temperatures and reflectivities are computed at the full resolution of the cloud model, that is, roughly 1 km in the horizontal and vertical. The relationship between the model-resolution brightness temperatures/radar reflectivities and the sensor-measured quantities is given by

$$y_s = \frac{1}{G} \int_{\Omega} \gamma(\theta, \phi) y_m(\theta, \phi) \sin(\theta) d\theta d\phi, \quad (7)$$

where

$$G = \int_{\Omega} \gamma(\theta, \phi) \sin(\theta) d\theta d\phi. \quad (8)$$

Here, y_s is one of the simulated sensor measurements and y_m is the corresponding model-resolution quantity; γ is the angular sensitivity function of the sensor channel, and the integrals are over all solid angles Ω where the sensitivity function is nonnegligible. In this study, the AMPR sensitivity functions are approximated using Gaussian functions, which have the same half-power widths as the AMPR antenna patterns. The sensitivity function (two-way gain function) of the EDOP radar is prescribed as the square of the EDOP antenna pattern. All sensitivity functions are resampled at model grid-resolution by integrating the patterns over the surface model grid boxes.

c. The inversion method

In this development the vector \mathbf{x} is used to represent all of the physical quantities, including profiles of cloud and precipitation, to be retrieved using the inversion method, and the vector \mathbf{y}_0 represents the set of available sensor observations. Following Lorenc (1986), it is assumed that the “best” estimate of \mathbf{x} given the set of observations \mathbf{y}_0 is the expected value

$$\mathbf{E}(\mathbf{x}) = \iint \cdots \int \mathbf{x} \text{pdf}(\mathbf{x}) d\mathbf{x}, \quad (9)$$

where the probability density function $\text{pdf}(\mathbf{x})$ is proportional to the conditional probability that \mathbf{x} represents

the true earth/atmosphere state, \mathbf{x}_{true} , given that \mathbf{y} is equal to the observed \mathbf{y}_0 ,

$$\text{pdf}(\mathbf{x}) \propto P(\mathbf{x} = \mathbf{x}_{\text{true}} | \mathbf{y} = \mathbf{y}_0). \quad (10)$$

The multiple integral signs in Eq. (9) indicate integration over all dimensions of the state vector \mathbf{x} .

Using Bayes's theorem (again following Lorenc 1986), the relation Eq. (10) may be rewritten as

$$\text{pdf}(\mathbf{x}) \propto P(\mathbf{y} = \mathbf{y}_0 | \mathbf{x} = \mathbf{x}_{\text{true}}) P(\mathbf{x} = \mathbf{x}_{\text{true}}) \quad (11)$$

$$\propto P_{\text{OS}}[\mathbf{y}_0 - \mathbf{y}_s(\mathbf{x})] P_a(\mathbf{x}), \quad (12)$$

where P_{OS} is equivalent to the probability that the set of observations \mathbf{y}_0 deviate from the set of simulated observations $\mathbf{y}_s(\mathbf{x})$ by a certain amount, given the earth/atmosphere state \mathbf{x} , and P_a is the a priori probability that \mathbf{x} is the true state of the earth/atmosphere. If it is assumed that the errors in the observations and the simulated observations are Gaussian and uncorrelated, then the probability of observational deviation can be expressed as

$$P_{\text{OS}}[\mathbf{y}_0 - \mathbf{y}_s(\mathbf{x})] \propto \exp\{-0.5[\mathbf{y}_0 - \mathbf{y}_s(\mathbf{x})]^T \times (\mathbf{O} + \mathbf{S})^{-1}[\mathbf{y}_0 - \mathbf{y}_s(\mathbf{x})]\}, \quad (13)$$

where \mathbf{O} and \mathbf{S} are the observation and simulation error covariance matrices, respectively. Substituting for P_{OS} in Eq. (12) using Eq. (13), and then using the resulting expression to substitute for $\text{pdf}(\mathbf{x})$ in Eq. (9), the final expression for the expected value of \mathbf{x} is

$$\mathbf{E}(\mathbf{x}) = \iiint \cdots \int \mathbf{x} \frac{\exp\{-0.5[\mathbf{y}_0 - \mathbf{y}_s(\mathbf{x})]^T \times (\mathbf{O} + \mathbf{S})^{-1}[\mathbf{y}_0 - \mathbf{y}_s(\mathbf{x})]\}}{A} \times P_a(\mathbf{x} = \mathbf{x}_{\text{true}}) d\mathbf{x}, \quad (14)$$

where A is a normalization factor,

$$A = \iiint \cdots \int \exp\{-0.5[\mathbf{y}_0 - \mathbf{y}_s(\mathbf{x})]^T (\mathbf{O} + \mathbf{S})^{-1} \times [\mathbf{y}_0 - \mathbf{y}_s(\mathbf{x})]\} P_a(\mathbf{x} = \mathbf{x}_{\text{true}}) d\mathbf{x}. \quad (15)$$

At this stage it is common practice in remote sensing applications to reexpress P_a as the probability of the deviation of \mathbf{x} from some suitable initial guess state \mathbf{x}_{in} , and then assume that the resulting probability $P_{\text{in}}(\mathbf{x} - \mathbf{x}_{\text{in}})$ has a Gaussian form. It follows that the minimum variance solution is equivalent to the state \mathbf{x} that minimizes the functional

$$J(\mathbf{x}) = [\mathbf{y}_0 - \mathbf{y}_s(\mathbf{x})]^T (\mathbf{O} + \mathbf{S})^{-1} [\mathbf{y}_0 - \mathbf{y}_s(\mathbf{x})] + (\mathbf{x} - \mathbf{x}_{\text{in}})^T \mathbf{I}^{-1} (\mathbf{x} - \mathbf{x}_{\text{in}}), \quad (16)$$

where \mathbf{I} is the error covariance matrix of the initial guess \mathbf{x}_{in} (see, e.g., Eyre 1989).

This method of solution requires an iterative search for the minimum of the scalar J in the multidimensional space of \mathbf{x} , which involves the evaluation of the partial

derivatives of \mathbf{y}_s at the current iterate of \mathbf{x} . Although it is widely used, this approach is not practical in the applications that follow. First, the evaluation of \mathbf{y}_s or its derivatives is computationally intensive, and since in general the components of \mathbf{y}_s are nonlinear functions of the vector components of \mathbf{x} , the derivatives should be evaluated on each iteration. Typically, \mathbf{x} can have a dimension of 10 or greater, and \mathbf{y}_s is also about 10 in many applications; so about 100 or more evaluations of \mathbf{y}_s or its derivatives would be required on each iteration. In addition, for a given set of observations, J may have a shallow minimum or even multiple minima, which can complicate the search procedure. Another consideration is that in the applications of this study, the a priori probability distribution $P_a(\mathbf{x} = \mathbf{x}_{\text{true}})$, in which the components of \mathbf{x} are typically hydrometeor water contents at different levels of the atmosphere, is decidedly non-Gaussian. Hydrometeor water contents usually follow a mixed lognormal probability distribution (Kedem et al. 1994).

The alternative approach taken in the present study is to make an approximate evaluation of the integral expression for the expected value of \mathbf{x} , Eq. (14). First, a sufficiently large database of atmospheric profiles and associated brightness temperatures/radar reflectivities is generated using the output of the GCE model in conjunction with the forward passive and active microwave radiometer models (see sections 2a and 2b). For the purpose of future discussion this database will be called the "supporting" cloud/radiative model database. The impact of the supporting database size and diversity of atmospheric profiles on the accuracy of profile retrievals is examined in the next section. Employing the large supporting cloud/radiative model database, $\mathbf{E}(\mathbf{x})$ in Eq. (14) can be approximated by

$$\hat{\mathbf{E}}(\mathbf{x}) = \sum_j \mathbf{x}_j \frac{\exp\{-0.5[\mathbf{y}_0 - \mathbf{y}_s(\mathbf{x}_j)]^T \times (\mathbf{O} + \mathbf{S})^{-1}[\mathbf{y}_0 - \mathbf{y}_s(\mathbf{x}_j)]\}}{\hat{A}}, \quad (17)$$

where \hat{A} is the normalization factor

$$\hat{A} = \sum_j \exp\{-0.5[\mathbf{y}_0 - \mathbf{y}_s(\mathbf{x}_j)]^T \times (\mathbf{O} + \mathbf{S})^{-1}[\mathbf{y}_0 - \mathbf{y}_s(\mathbf{x}_j)]\}. \quad (18)$$

The integrals in Eqs. (14) and (15) are replaced by the summations in Eqs. (17) and (18) over all model-simulated profiles \mathbf{x}_j in the supporting cloud/radiative model database. Here, the main assumption is that profiles in the supporting database occur with nearly the same relative frequency as those found in nature, or at least with the same frequency as those found in the region where the retrieval method is to be applied. Under this assumption, the weighting by $P_a(\mathbf{x} = \mathbf{x}_{\text{true}})$ in the integral form Eq. (14) is represented simply by the relative number of occurrences of a given profile type \mathbf{x}_j in the summation Eq. (17). Since the atmospheric

profiles are generated using a model that incorporates most relevant physical processes of the earth and atmosphere, the relative frequency of simulated profiles of a certain type should be roughly the same as that of naturally occurring profiles if (a) the atmospheric model is used to simulate cloud development over the range of environments observed in the region of interest, and (b) that each cloud model simulation is sampled at regular time intervals, such that no particular stage of cloud or cloud system development is favored over another. Ideally, these conditions should be satisfied; however, in practice only a limited number of cloud model simulations may be available for constructing the supporting cloud/radiative model database. In fact, even a large supporting database may not include all of the environments encountered by the radiometer–radar system.

The question may then be posed: Can the retrieval method still provide useful estimates of cloud/precipitation profiles where the atmospheric environment is somewhat different from the environments of the cloud model simulations that contribute to the supporting database? The answer to this question is that it may still be possible to obtain reasonable solutions from the retrieval method if there exist *individual* cloud/precipitation profiles in the supporting database similar to those observed by the sensor. The existence of viable profiles in the supporting database can be determined by looking at the root-mean-square deviation between the brightness temperatures/reflectivities associated with the retrieved profile and the observed brightness temperatures/reflectivities. If the rms deviation is on the order of (or less than) the combined error of the simulated and observed brightness temperatures/reflectivities, then the retrieved profile is viable; otherwise, a profile “radiatively” consistent with the observations does not exist in the supporting database. However, even if the retrieved profile is not quite a proper match to the observations, it may be close to a match and, therefore, might be useful if the error in the retrieved profile is tolerable for a given application. Again, the rms deviation between the brightness temperatures/reflectivities associated with the retrieved profile and the observed brightness temperatures/reflectivities is a useful measure of the quality of the retrieved profile. The greater the rms deviation, the greater the uncertainty in the retrieved profile.

Another possibility is that a cloud model simulation is run for the environment where the retrieval method is applied, but errors in the model simulation lead to erroneous cloud and precipitation profiles that enter the supporting cloud/radiative model database. These erroneous profiles will not necessarily contribute to the retrieval solution, since the exponential term in Eq. (17) ensures that profiles must be radiatively consistent with the observations to contribute.

A much more complex issue that impacts all retrievals is that of the uniqueness of the retrieved profile.

Even if the supporting database includes a full spectrum of possible cloud/precipitation profiles, the radiometer/radar observations may be compatible with several different profiles, and so the actual profile may not be uniquely identified. One measure of nonuniqueness is the variance of a retrieved parameter, given a set of observations. The covariance matrix of \mathbf{x} may be estimated, following Papoulis (1965),

$$\hat{\mathbf{V}}(\mathbf{x}) = \hat{\mathbf{E}}\{[\mathbf{x} - \hat{\mathbf{E}}(\mathbf{x})][\mathbf{x} - \hat{\mathbf{E}}(\mathbf{x})]^T\}. \quad (19)$$

Since the diagonal elements of $\hat{\mathbf{V}}(\mathbf{x})$ give the deviation of \mathbf{x} from its “retrieved” value, they are a measure of the uncertainty in \mathbf{x} based upon the supporting cloud/radiative model database. The impact of the supporting database on retrievals is examined using synthetic data in the next section.

3. Application to AMPR and EDOP

a. Instrument descriptions

The Advanced Microwave Precipitation Radiometer (AMPR) is a scanning passive microwave radiometer with channels at 10.7, 19.35, 37.1, and 85.5 GHz. A full description of the AMPR instrument can be found in Spencer et al. (1994). The NASA ER-2 Doppler radar (EDOP) is an X-band (9.72 GHz) Doppler radar with fixed nadir and forward-looking beams (Heymsfield et al. 1993). Basic specifications of the AMPR and EDOP are listed in Table 1.

To facilitate collocation of passive and active microwave measurements from the AMPR and EDOP, only the nadir-view data from these instruments are considered. At nadir view, the half-power surface footprint dimensions of the AMPR are 2.8 km, 2.8 km, 1.5 km, and 0.6 km for the 10.7-, 19.35-, 37.1-, and 85.5-GHz channels, respectively. A 10.7-GHz channel resolution equal to the 19.35-GHz resolution is achieved using a separate 24.6-cm-diameter antenna; all of the other channels utilize a 13.5-cm antenna. Nadir observations from the EDOP employ a 76-cm-diameter antenna with a 2.9° beamwidth, yielding a surface resolution of approximately 1.0 km. The EDOP data utilized in this study have a vertical resolution of 150 m, and with the ER-2 flying at a nominal altitude of 20 km, the nadir-view minimum detectable signal is approximately 8 dBZ at 10-km altitude and 14 dBZ at the surface.

b. Synthetic retrievals

In this subsection, the retrieval method is tested using simulated AMPR and EDOP observations generated from the GCE model and the forward passive and active radiometer models described in section 2. The purpose of these tests is to provide a benchmark for expected errors in retrieved cloud/precipitation profiles, and to determine how sensitive these errors are to (a) the type of sensor data utilized, (b) the background surface, (c) errors in the summation approximation

(Eq. 17), (d) the type of supporting cloud/radiative model data employed, and (e) errors in the observations.

The use of simulated data in these retrieval experiments makes it possible to initially evaluate algorithm performance under controlled conditions. If these retrieval method tests were performed on actual radiometer/radar data, comparing the resulting retrieved profiles to independent ground truth data, then random errors and biases inherent to the retrieval method itself could not be distinguished from random errors and biases in the ground truth data, or from errors in the radiometer/radar observations and cloud/radiative model simulations. Independent ground "truth" data, such as volume-scan radar data, are subject to errors in radar operation and calibration, as well as errors resulting from space and time offsets between the aircraft radiometer/radar and validation radar measurements.

Although there are certain advantages gained from the controlled conditions in synthetic retrieval tests, these tests are only meant to augment future retrieval validation studies, which utilize quality ground truth. Since the retrieval method provides estimates of the water content profiles of several hydrometeor species, in situ probe measurements of cloud and precipitation water contents at different altitudes coinciding with volume-scan radar observations would be optimal for validation studies. Presently, there is a dearth of such data, and none are available for the EDOP measurement campaigns.

A relatively small portion of the combined GATE and TOGA COARE GCE model simulations is segregated from the rest of the simulations to serve as synthetic data. A subset of the AMPR brightness temperatures and EDOP reflectivities derived from the GCE model-simulated TOGA COARE atmospheric profiles at 210 min are utilized as synthetic observations. First, model profiles/brightness temperatures/radar reflectivities are sampled every three horizontal grid points (every 3 km) in both the X and Y directions from the 210-min TOGA COARE simulation. Although model profiles at 3-km spacing are not independent, there is negligible overlap of the simulated observations at this spacing, since the maximum footprint dimension of the observations is 2.8 km. Also, in order to emphasize significant precipitation water contents in the statistics, only brightness temperature/reflectivity simulations corresponding to profiles having vertically integrated precipitation (rain, snow, and graupel) amounts greater than or equal to 1.0 kg m^{-2} are selected as synthetic observations. A total of 182 profiles and associated observations from the sampled model domain satisfying the integrated precipitation threshold are extracted. Since four brightness temperature/radar reflectivity simulations are computed for each atmospheric profile over both water and land surface backgrounds (see section 2b), a total of 728 synthetic radiometer/radar observations are created for both water and land surfaces.

In each synthetic retrieval test to follow, the retrieval method is applied to the synthetic observations, and estimates of the integrated precipitating liquid, integrated precipitating ice (snow and graupel), and surface rain rate from the retrieved profile (approximately $1 \text{ km} \times 1 \text{ km}$ resolution) centered on the observations are computed. Error statistics of the retrieved quantities are determined by comparing them to the known quantities from the GCE model synthetic database. All statistics are stratified by surface type (simulations over water and land surfaces) and instruments used (either the AMPR data only, EDOP data only, or combined AMPR and EDOP data). A total of 728 retrievals are performed on the synthetic observations over both water and land surfaces in each test. The mean integrated precipitating liquid of the synthetic dataset profiles is 1.99 kg m^{-2} , while the mean integrated precipitating ice (snow and graupel) is 1.12 kg m^{-2} , and the mean surface rain rate is 8.34 mm h^{-1} .

1) BASELINE RETRIEVAL TESTS

In the following baseline retrieval tests, all profiles and simulations of AMPR brightness temperatures and EDOP reflectivities generated from the GATE and TOGA COARE GCE model runs (other than the time 210 TOGA COARE data) are utilized in the supporting database of the retrieval method. Nominal noise is added to both the synthetic AMPR and EDOP data. To the AMPR data, zero-mean Gaussian distributed noise with a standard deviation of 1.5 K is added to the data from each channel using a random number generator. This noise level is derived from the measured values in Spencer et al. (1994), but is increased according to information from R. Hood (1994, personal communication) regarding additional uncertainty in the calibration of the AMPR during CAMEX. For EDOP, random errors with a variance of $0.0328Z^2$ are added to the radar reflectivities. Consistent with the operation of the EDOP during CAMEX, this error variance is derived for a logarithmic radar receiver that averages 50 independent samples of return power per measurement (Sauvageot 1992).

To apply the retrieval method, appropriate magnitudes for the error covariance matrices, \mathbf{O} and \mathbf{S} in Eq. (17), must be determined. In the synthetic retrievals the forward radiative model $\mathbf{y}_s(\mathbf{x})$ is exact, and so the error covariance matrix \mathbf{S} yields no contribution. Also, due to lack of information on the correlation of errors between instruments and between channels of the same instrument, only the diagonal terms of the matrix \mathbf{O} will be estimated in the present study; all off-diagonal terms are set to zero. The assumed observation error variances are set equal to the nominal instrument error variances estimated previously. Statistics of the baseline retrieval tests that utilize these nominal noise error variances are indicated by $\sigma_0 = \sigma_n$ in Table 2 (over water surfaces) and Table 3 (over land surfaces).

TABLE 2. Statistics of AMPR-only, EDOP-only, and AMPR + EDOP synthetic retrievals over four water surfaces. Listed are the bias, error standard deviation σ_e , and correlation coefficient r of retrievals for different variations of the retrieval method. The bias and σ_e have units of kilograms per square meter for integrated precipitating liquid and ice, and millimeters per hour for surface rain rate. Capital letters refer to the supporting cloud/radiative model database used in the retrieval; G indicates a retrieval using the GATE supporting database only, T indicates a retrieval using the TOGA COARE supporting database, and C indicates usage of the combined GATE plus TOGA COARE supporting database. Two sigma values in sequence are also listed for each retrieval: the first indicates the error standard deviation of noise added to the observations prior to the retrieval; the second is the observational error standard deviation assumed in the retrieval [Eq. (17)].

			Precipitating liquid			Precipitating ice			Surface rain rate		
			Bias	σ_e	r	Bias	σ_e	r	Bias	σ_e	r
AMPR-only											
C	σ_n	σ_n	-0.07	0.64	0.978	-0.06	0.37	0.931	-0.55	4.58	0.953
C	σ_n	$2\sigma_n$	-0.08	0.73	0.972	-0.08	0.38	0.931	-0.52	4.42	0.958
C	σ_n	$4\sigma_n$	-0.09	0.91	0.954	-0.11	0.45	0.906	-0.41	4.70	0.951
C	σ_n	$8\sigma_n$	-0.12	1.08	0.936	-0.11	0.58	0.861	-0.47	5.12	0.946
G	σ_n	$2\sigma_n$	-0.06	1.39	0.879	-0.14	0.70	0.731	+2.94	13.39	0.602
T	σ_n	$2\sigma_n$	-0.09	0.73	0.972	-0.07	0.38	0.927	-0.65	4.36	0.959
C	$2\sigma_n$	$2\sigma_n$	-0.07	0.80	0.965	-0.07	0.43	0.905	-0.41	4.75	0.949
EDOP-only											
C	σ_n	σ_n	-0.16	0.38	0.991	-0.09	0.20	0.982	-0.87	4.07	0.962
C	σ_n	$2\sigma_n$	-0.19	0.55	0.987	-0.09	0.19	0.986	-1.05	4.16	0.966
C	σ_n	$4\sigma_n$	-0.26	0.74	0.976	-0.11	0.18	0.989	-1.52	5.24	0.947
C	σ_n	$8\sigma_n$	-0.62	1.59	0.881	-0.26	0.34	0.972	-3.32	8.38	0.892
G	σ_n	$2\sigma_n$	-0.64	1.80	0.781	+0.11	0.51	0.886	-3.50	10.64	0.691
T	σ_n	$2\sigma_n$	-0.19	0.55	0.987	-0.09	0.19	0.986	-1.05	4.16	0.966
C	$2\sigma_n$	$2\sigma_n$	-0.70	1.99	0.748	-0.27	0.46	0.928	-3.45	10.60	0.707
AMPR + EDOP											
C	σ_n	σ_n	-0.16	0.48	0.985	-0.10	0.21	0.979	-0.68	4.61	0.950
C	σ_n	$2\sigma_n$	-0.15	0.46	0.987	-0.10	0.21	0.980	-0.69	4.45	0.953
C	σ_n	$4\sigma_n$	-0.16	0.41	0.990	-0.12	0.19	0.984	-0.82	4.13	0.960
C	σ_n	$8\sigma_n$	-0.23	0.47	0.987	-0.24	0.28	0.975	-1.17	4.61	0.951
G	σ_n	$2\sigma_n$	-0.65	1.59	0.846	-0.06	0.41	0.916	-2.88	9.90	0.739
T	σ_n	$2\sigma_n$	-0.15	0.46	0.987	-0.10	0.21	0.980	-0.69	4.45	0.953
C	$2\sigma_n$	$2\sigma_n$	-0.51	1.31	0.889	-0.30	0.45	0.932	-2.46	9.09	0.786

It may be inferred from Table 2 that over water surfaces, retrieval estimates of either integrated precipitating liquid, integrated precipitating ice, or surface rain rate are well-correlated with the true values, although retrieval random errors are significant. The retrieval of integrated precipitating ice using the AMPR data yields a minimum correlation of 0.931, while all of the other retrievals yield correlations above 0.950. On the other hand, error standard deviations of the retrievals, defined as percentages of the mean by $\sigma_e/\text{mean} \times 100\%$, range from 18% to 55%. Total biases in the retrievals are always negative and less than 10% of the mean values. Retrievals using the EDOP data and the combined AMPR + EDOP data generally have lower random errors than the AMPR-only retrievals, with the exception of retrieved surface rain rate. Conversely, biases in the retrievals based upon the EDOP and combined AMPR + EDOP data are always slightly greater in magnitude relative to the AMPR-only retrievals.

Over land surfaces (Table 3), the EDOP retrieval statistics are identical to those over water, since the synthetic radar data are independent of surface type. AMPR retrievals of integrated precipitating liquid and rain rate are considerably less accurate than those over water. This result follows from the fact that the liquid precipitation primarily absorbs and emits microwave radiances at the AMPR frequencies, and this absorption/emission cannot be easily distinguished from the high-emissivity land backgrounds. Conversely, the scattering signature of precipitating ice is easily detected over the highly emissive land surface backgrounds, and so the accuracy of AMPR retrievals of integrated precipitating ice is comparable to that over water. Retrievals over land using the AMPR and EDOP together are not significantly different from the EDOP-only retrievals, suggesting that the accuracy of the combined retrievals is primarily limited by the information contained in the EDOP data. Also, the accuracy of the combined

TABLE 3. Same as Table 2 but for synthetic retrievals over four land surfaces.

			Precipitating liquid			Precipitating ice			Surface rain rate		
			Bias	σ_e	r	Bias	σ_e	r	Bias	σ_e	r
AMPR-only											
C	σ_n	σ_n	-0.04	1.18	0.912	-0.05	0.37	0.934	-0.47	6.97	0.884
C	σ_n	$2\sigma_n$	-0.07	1.31	0.896	-0.08	0.39	0.925	-0.57	7.36	0.876
C	σ_n	$4\sigma_n$	-0.17	1.72	0.852	-0.11	0.46	0.905	-1.23	9.20	0.846
C	σ_n	$8\sigma_n$	-0.22	2.36	0.762	-0.12	0.62	0.828	-1.81	12.45	0.759
G	σ_n	$2\sigma_n$	-0.36	1.93	0.827	-0.25	0.45	0.904	-0.08	10.23	0.791
T	σ_n	$2\sigma_n$	-0.07	1.29	0.899	-0.06	0.39	0.924	-0.68	7.29	0.877
C	$2\sigma_n$	$2\sigma_n$	-0.02	1.52	0.847	-0.06	0.45	0.899	-0.26	8.40	0.822
EDOP-only											
C	σ_n	σ_n	-0.16	0.38	0.991	-0.09	0.20	0.982	-0.87	4.07	0.962
C	σ_n	$2\sigma_n$	-0.19	0.55	0.987	-0.09	0.19	0.986	-1.05	4.16	0.966
C	σ_n	$4\sigma_n$	-0.26	0.74	0.976	-0.11	0.18	0.989	-1.52	5.24	0.947
C	σ_n	$8\sigma_n$	-0.62	1.59	0.881	-0.26	0.34	0.972	-3.32	8.38	0.892
G	σ_n	$2\sigma_n$	-0.64	1.80	0.781	+0.11	0.51	0.886	-3.50	10.64	0.691
T	σ_n	$2\sigma_n$	-0.19	0.55	0.987	-0.09	0.19	0.986	-1.05	4.16	0.966
C	$2\sigma_n$	$2\sigma_n$	-0.70	1.99	0.748	-0.27	0.46	0.928	-3.45	10.60	0.707
AMPR + EDOP											
C	σ_n	σ_n	-0.15	0.38	0.991	-0.09	0.21	0.981	-0.87	4.15	0.960
C	σ_n	$2\sigma_n$	-0.15	0.34	0.993	-0.09	0.20	0.983	-0.79	3.95	0.963
C	σ_n	$4\sigma_n$	-0.21	0.42	0.992	-0.11	0.18	0.987	-1.23	4.59	0.953
C	σ_n	$8\sigma_n$	-0.54	1.28	0.940	-0.23	0.28	0.978	-2.96	7.38	0.921
G	σ_n	$2\sigma_n$	-0.61	1.62	0.840	-0.02	0.43	0.909	-3.34	10.32	0.717
T	σ_n	$2\sigma_n$	-0.15	0.34	0.993	-0.10	0.20	0.983	-0.79	3.95	0.963
C	$2\sigma_n$	$2\sigma_n$	-0.68	2.00	0.725	-0.25	0.41	0.944	-3.27	10.84	0.675

AMPR + EDOP retrievals over land is about the same as that over water.

2) SENSITIVITY TO SUMMATION APPROXIMATION ERRORS

Although there is a formal accounting for observation and simulation errors in the retrieval method, there are additional errors in the retrievals due to the fact that the finite sum over the supporting cloud/radiative model data in Eq. (17) is only an approximation to the integral in Eq. (14). In neighborhoods of y_0 where few simulations $y_s(x)$ exist, the summation approximation to the integral will be poor.

This effect is illustrated in Fig. 4. Imagine a ‘single-channel’ retrieval that utilizes only error-free 10.7-GHz brightness temperature data from the AMPR to estimate the integrated precipitating liquid from Eq. (17). If an observational error standard deviation of σ_0 is specified, then for an AMPR brightness temperature observation of 250 K, Eq. (17) yields roughly the mean of all the integrated liquid precipitation amounts in the supporting cloud/radiative model database associated with brightness temperatures within the $250 \pm \sigma_0$ K bounds. Bounds for $\sigma_0 = 0.5\sigma_n$ (0.75 K) and $\sigma_0 = 2.0\sigma_n$ (3.0 K) are illustrated in Fig. 4a, against the supporting data (circular dots). If Eq. (17) is applied to all of the

possible observations of 10.7-GHz brightness temperatures between 125 and 275 K, then the dotted ($\sigma_0 = 0.5\sigma_n$) and solid ($\sigma_0 = 2.0\sigma_n$) curves of Fig. 4b result. It can be seen that if a relatively small $0.5\sigma_n$ is specified, the estimated integrated precipitating liquid can fluctuate considerably as the observed brightness temperature increases, which suggests that there are too few data (especially at high integrated precipitation amounts) present within the small ± 0.75 -K interval to make a reliable approximation to the mean value using Eq. (17). A better approximation can be obtained by specifying $\sigma_0 = 2.0\sigma_n$. In this case a much smoother, more realistic approximation to the mean value is obtained.

A similar result is obtained if one considers the single-channel EDOP retrieval illustrated in Fig. 5. In Fig. 5a the mean radar reflectivity between the surface and 5-km altitude is plotted against the associated integrated precipitating liquid. If a mean reflectivity of 42 dBZ is observed, then the noise deviations $\pm 0.5\sigma_n$ and $\pm 2.0\sigma_n$ are shown as dotted and solid lines, respectively, in the panel. Assuming these two error standard deviations, the relationships implied by Eq. (17) between the observed reflectivities and mean integrated precipitating liquid amounts are shown in Fig. 5b. Here, again, there are small fluctuations in the relationship that utilizes the smaller

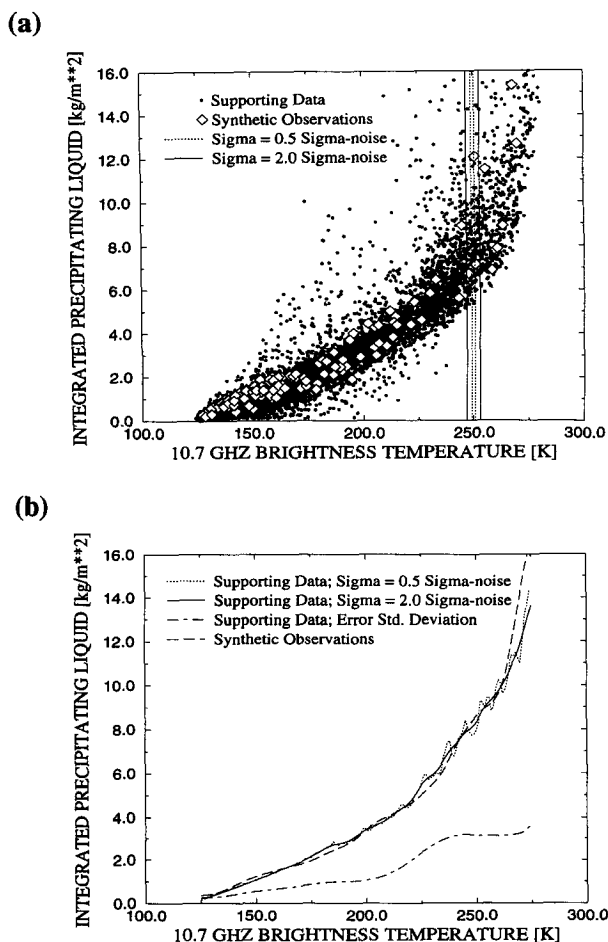


FIG. 4. Brightness temperature single-channel retrieval plots. (a) The scatterplot of integrated precipitating liquid as a function of 10.7-GHz brightness temperature from the supporting cloud/radiative model database (dots) and synthetic observations from the 210-min TOGA COARE simulation (diamonds). For a brightness temperature measurement of 250 K, the dotted lines indicate the $\pm 0.5\sigma_n$ error range, and the solid lines indicate the $\pm 2.0\sigma_n$ error range. (b) The corresponding retrieval curves for $\sigma_0 = 0.5\sigma_n$ (dotted) and $\sigma_0 = 2.0\sigma_n$ (solid) computed using Eq. (17). The dot-dashed curve is the error standard deviation of the $\sigma_0 = 2.0\sigma_n$ retrieval curve estimated from the supporting database and Eq. (19). The long-dashed line is the retrieval curve based upon the synthetic observations and Eq. (17).

$\sigma_0 = 0.5\sigma_n$ standard deviation, while if the larger $\sigma_0 = 2.0\sigma_n$ is assumed, then a smoother relationship results.

The single channel tests suggest that by inserting a larger error standard deviation in the denominator of the exponential term of Eq. (17) one can help to compensate for errors in the summation approximation by broadening the neighborhood of y_0 , which effectively contributes to the summation. Of course, for some very high value of the specified error standard deviation the broadening of the neighborhood of y_0 will be too great, and the retrieval estimate $\hat{E}(x)$ will be biased toward the mean x of the supporting database. Although this

type of bias is not observed for the values of error standard deviation tested in this study, it has been observed in synthetic SSM/I retrievals performed by Kummerow et al. (1996).

In the following set of synthetic retrieval experiments, the assumed observational error standard deviations are augmented by factors of 2, 4, and 8 in an attempt to compensate for the additional error introduced by the retrieval method summation approximation. Results of these tests are indicated by $\sigma_0 = 2.0\sigma_n$, $4.0\sigma_n$, and $8.0\sigma_n$ in Tables 2 and 3. In most of the retrievals, there is at most only a slight improvement in retrieval accuracy for values of σ_0 greater than σ_n . In future tests an "optimal" $\sigma_0 = 2.0\sigma_n$ will be utilized.

3) DATABASE DEPENDENCE

It should be noted that the simulated observations in the synthetic retrieval tests are derived from one time

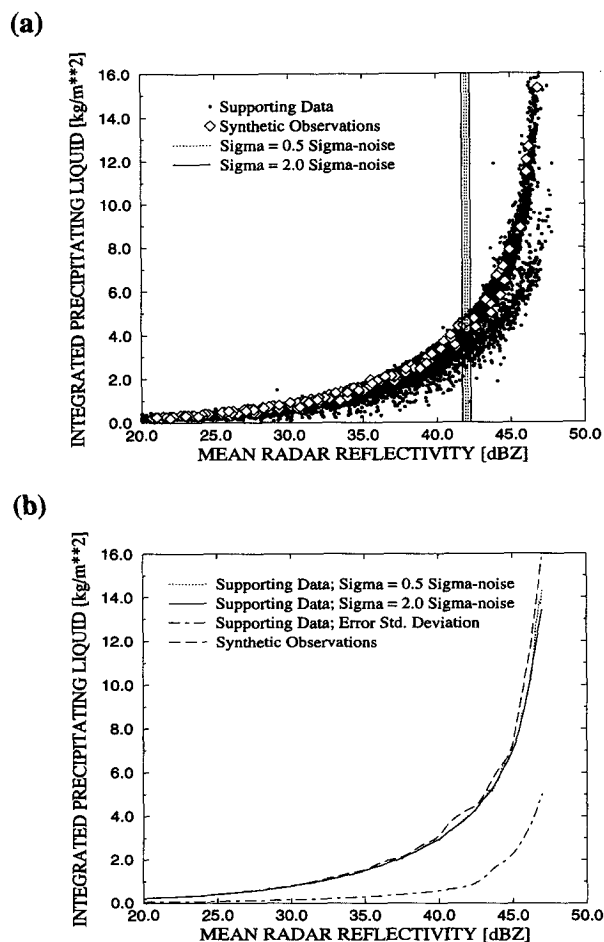


FIG. 5. Same as Fig. 4 but for the retrieval of integrated precipitating liquid using the mean 9.72-GHz radar reflectivity below 5-km altitude. Note that the error ranges in panel (a) are for a mean reflectivity measurement of 42 dBZ.

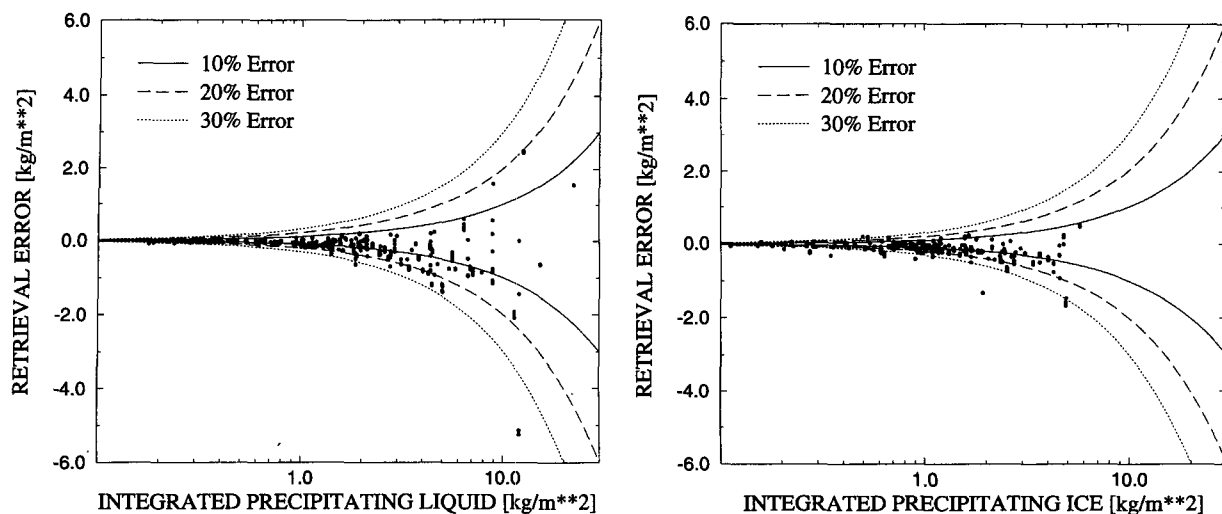


FIG. 6. Errors in the synthetic retrievals of integrated precipitating liquid (a), and integrated precipitating ice (b). The retrieval method is applied to synthetic AMPR and EDOP data derived from the 210-min TOGA COARE simulation over four water surface backgrounds.

period of the TOGA COARE model run, and, therefore, these observations correspond to profiles which may be similar to those of the supporting cloud/radiative model database, which includes a large number of TOGA COARE profiles. If instead the synthetic data included profiles coming from a very different atmospheric environment or climatic regime, then in principle it should be much more difficult to construct a realistic retrieval estimate of a given profile from a combination of supporting database profiles, as suggested by Eq. (17). In the following tests, retrievals are performed on the same set of synthetic observations (derived from the 210-min TOGA COARE GCE model simulation), while the supporting database of the retrieval method is changed. The first retrieval test, labeled "G" in Tables 2 and 3, incorporates only the GATE GCE model simulation data in the supporting database; the second retrieval test, labeled T, incorporates all of the TOGA COARE simulation data in the supporting database except for the 210-min stage. These two tests may be compared to the retrievals that utilize the combined (labeled "C") GATE and TOGA COARE GCE model simulations as supporting data, with $\sigma_0 = 2.0\sigma_n$ (second row).

It may be generally noted that when the GATE data are utilized to retrieve the subset of TOGA COARE precipitation water contents and surface rain rates, the accuracy of the retrievals is significantly lower than when either the TOGA COARE or combined GATE and TOGA COARE data are utilized as supporting data. Evidently, more accurate retrieved precipitation profiles can be constructed from a database that includes profiles that come from a similar, rather than a dissimilar, cloud environment.

This result is not surprising since the atmospheric environments used to initialize the GATE and TOGA

COARE GCE model simulations are different, even though both environments were taken from tropical observations. The initial stability, lifting profile, and vertical wind shear conditions in the GATE and TOGA COARE simulations are different, which might account for greater convective cell tilt and smaller ice to liquid precipitation ratios in the TOGA COARE simulations (W.-K. Tao 1995, personal communication). The precise mechanisms that account for these differences are not well understood, and are the subject of study at this time. The selection of supporting cloud/radiative model data appears to have a significant impact on all retrievals, with the possible exception of the AMPR-only retrievals of integrated precipitating ice over land. If the GATE supporting data are used exclusively in the retrievals, the retrieval errors (correlations) are generally much higher (lower) than those resulting from the use of TOGA COARE or combined supporting data; see Tables 2 and 3. This retrieval test emphasizes the importance of creating the most comprehensive supporting cloud/radiative model database possible for use in the retrieval method.

4) SENSITIVITY TO NOISE IN OBSERVATIONS

In a final synthetic retrieval experiment, the noise added to the simulated brightness temperatures/radar reflectivities of the synthetic dataset is doubled to examine the sensitivity of the retrieval method to larger observation error levels. The combined GATE and TOGA COARE simulations are utilized as supporting data in the retrievals. Statistics of this test are again logged in Tables 2 and 3. Over both water and land surfaces, the random errors in retrievals utilizing the EDOP or combined AMPR+EDOP data more than double when the noise is doubled. Retrievals using the

AMPR data alone degrade somewhat with the additional noise, but to a much lesser degree. For example, the random error in the EDOP retrievals of integrated precipitating liquid over water increase from a standard deviation of 28% to 100% of the mean value; combined AMPR + EDOP retrieval error standard deviations increase from 23% to 66%. Errors in the AMPR retrievals of integrated precipitating liquid increase from 37% to 40%. This result suggests that retrievals are much more sensitive to errors in the EDOP reflectivity data, and that specification of optimal σ_0 values based upon synthetic retrieval tests may be indicated for combined AMPR + EDOP retrievals.

5) ANALYSIS OF RANDOM ERRORS

Scatterplots of the errors in retrieved integrated precipitating liquid versus the actual integrated precipitating liquid, and errors in retrieved integrated precipitating ice versus actual integrated precipitating ice are shown in Fig. 6. These retrievals are performed using both the AMPR and EDOP data over water surfaces with an assumed error standard deviation $\sigma_0 = 2.0\sigma_n$. The distribution of errors in the AMPR + EDOP retrievals over land surfaces (not shown) are similar. Note that for significant integrated precipitating liquid and ice amounts, random errors in the retrievals increase with integrated precipitation amount. Percentage errors are generally less than 20% for integrated precipitating liquid and ice amounts greater than 1.0 kg m^{-2} .

The trend of retrieval error increasing with integrated precipitation amount can be understood by examining the single-channel retrievals in Figs. 4b and 5b. Note that the relationship between either the passive 10.7-GHz brightness temperatures or the active 9.72-GHz mean reflectivities and the integrated precipitating liquid amounts becomes more ambiguous as the integrated precipitation amount increases. The increasing ambiguity results in retrieval error standard deviations [evaluated from Eq. (19) and plotted as dot-dash lines in the figures] which increase with integrated precipitating liquid amount. The estimated errors in the passive 10.7-GHz and active 9.72-GHz single-channel estimates are on the order of 35% and 25%, respectively, for precipitating liquid amounts greater than 1.0 kg m^{-2} .

The single-channel retrievals are a good analog to the multichannel estimates, since all of the AMPR and EDOP channels lose sensitivity as the precipitation amount becomes large. Note that the theoretical estimates of the single-channel retrieval random errors computed using Eq. (19) and plotted as dot-dash curves in Figs. 4b and 5b also increase with increasing integrated precipitating liquid amount, but percentage errors are relatively constant with precipitation amount. Dividing the error standard deviations of the AMPR + EDOP retrieved quantities from Tables 2 and

3 ($\sigma_0 = 2\sigma_n$ case; second row) by the true mean quantities, retrieval random errors of 23%, 19%, and 53% are obtained for estimates of integrated precipitating liquid, integrated precipitating ice, and surface rain rate, respectively. The percentage errors of the retrieved quantities over water and land surfaces are similar, and the maximum percentage errors are used here.

It has been shown by Tao et al. (1993) that vertical distributions of latent heating are linked to vertical hydrometeor distributions. Especially important is the classification of precipitation as convective or stratiform. Convective rain is generally characterized by heating in the lower troposphere, while stratiform precipitation is usually associated with heating in the upper troposphere (above the freezing level) and cooling in the lower troposphere (below the freezing level).

The method of Churchill and Houze (1984) is employed here to discriminate between convective and stratiform regions in the 210-min TOGA COARE squall-line simulation. Of the 728 synthetic observations over water backgrounds described previously, 360 are from convective regions and 320 are from stratiform regions. The remaining 48 are too close to the model boundary for proper classification and are, therefore, eliminated from the following analysis. The retrieval method is applied separately to the sets of synthetic AMPR brightness temperatures and EDOP reflectivities from the convective and stratiform regions. In Fig. 7 the mean retrieved convective and stratiform profiles of total precipitation (rain, snow, and graupel)

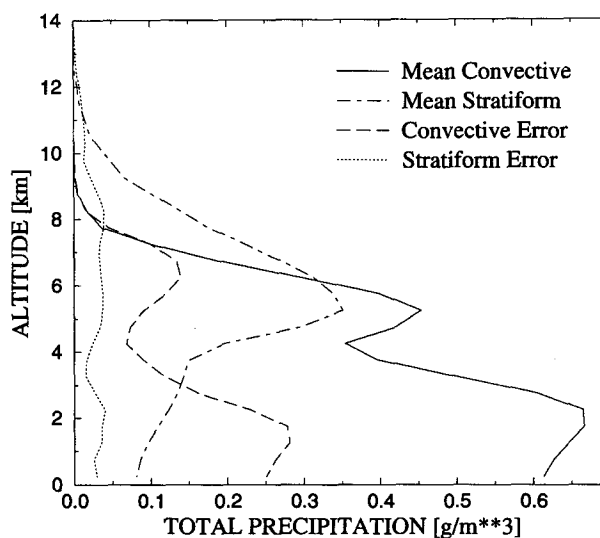
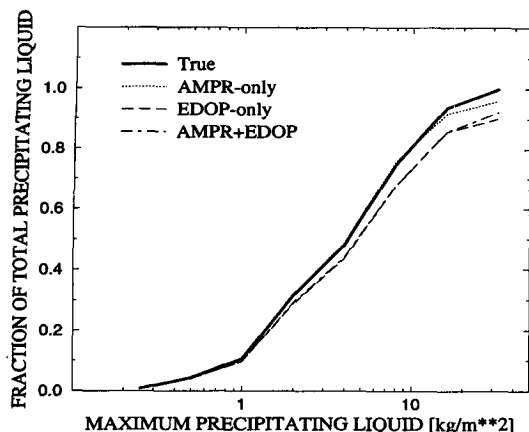


FIG. 7. Mean vertical profiles of retrieved total precipitation (rain, snow, and graupel) and retrieval error standard deviation based upon the convective and stratiform regions of the 210-min TOGA COARE model simulation. Convective and stratiform regions are distinguished using the Churchill and Houze (1984) technique. The retrieval method is applied to synthetic AMPR and EDOP data derived from the 210-min TOGA COARE simulation over four water surface backgrounds.

(a)



(b)

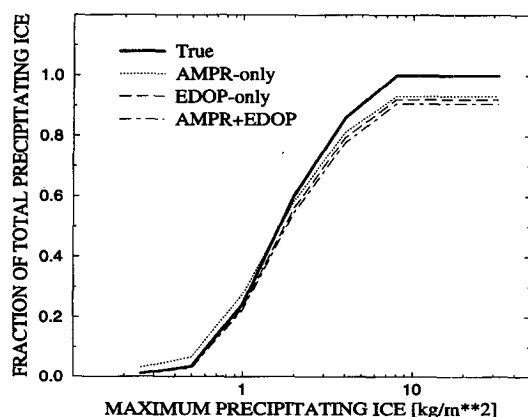


FIG. 8. Cumulative distributions of integrated precipitating liquid (a), and integrated precipitating ice (b). Solid lines indicate the known distributions from the 210-min TOGA COARE cloud model simulation; dotted lines are the cumulative distributions of quantities retrieved using the synthetic AMPR data only [see Eq. (20)]; long-dashed and dash-dot lines are the cumulative distributions of quantities retrieved using synthetic EDOP data only and synthetic AMPR + EDOP data, respectively. Synthetic AMPR and EDOP data are derived from the 210-min TOGA COARE simulation over four water surface backgrounds.

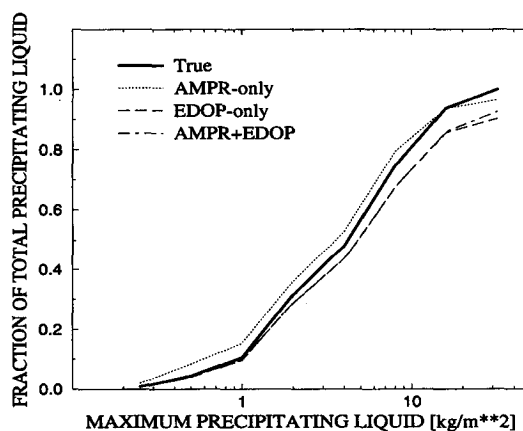
and retrieval error standard deviations from this test are plotted. Note that the bulk of the precipitation in convective regions resides below 8 km, while most of the stratiform precipitation lies between 4 and 10 km, with a maximum near 6 km. AMPR + EDOP retrieval errors in convective regions typically increase with the mean precipitation water content at a given level, while retrieval errors in stratiform regions are nearly constant with height. Also, retrieval errors associated with convective precipitation are generally greater than those associated with stratiform rain, again reflecting the correlation between error and mean water content. Statistics of AMPR + EDOP retrievals of convective and

stratiform profiles from the same hydrometeor distributions over land surfaces (not shown) are very similar to those over water.

6) ANALYSIS OF BIASES

The preceding analysis has focused on the comparison of retrieval random errors, and the correlations between retrieved and true precipitation variables. These statistics are especially important in aircraft studies of the high-resolution, instantaneous structure of individual storms or convective systems. In future studies the authors will apply the combined passive-active microwave retrieval method to data from satellite-borne passive and active radiometers, such as the TRMM Microwave Imager and Precipitation Radar to be flown on the TRMM satellite. Continuously operating satellite-borne radiometers can provide the data needed for climate studies, since larger space and time averages of retrieved quantities are required for climate work. In

(a)



(b)

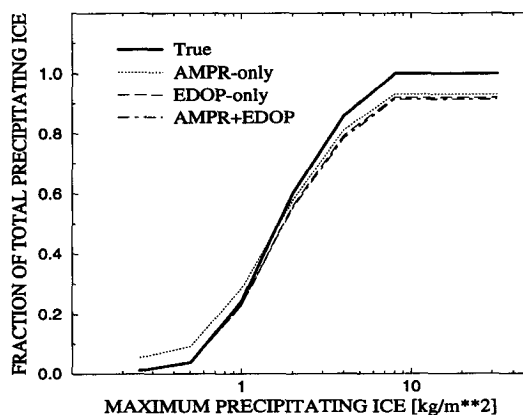


FIG. 9. Same as Fig. 8 but for retrievals over land surface backgrounds.

space and time averages of retrievals, the influence of random errors is dramatically reduced by oversampling; however, biases in the retrievals are not reduced in this way.

Shown in Figs. 8 and 9 are the cumulative fraction distributions of integrated precipitating liquid and integrated precipitating ice, as well as the cumulative fraction distributions from synthetic retrievals using the AMPR, EDOP, and combined AMPR + EDOP observations with $\sigma_0 = 2.0\sigma_n$. The cumulative fraction is defined

$$\text{CumFrac}(x, x_{\max}) \equiv \frac{\sum_j (x_j | x_{\text{true}_j} \leq x_{\max})}{\sum_j x_{\text{true}_j}}, \quad (20)$$

where x_j and x_{true_j} are components of the retrieved quantity vector $\hat{\mathbf{E}}(\mathbf{x})_j$ and the corresponding true vector $\mathbf{x}_{\text{true}_j}$, respectively, and x_{\max} is the maximum true value indicated on the abscissa of each plot in the figure. Thus, the difference of the retrieved and true cumulative fractions of x provides a measure of the bias of the retrieved x for the subset of true values less than x_{\max} . The cumulative fraction distributions of the retrieved quantities are compared to the true fraction distributions shown as darker lines in the figures.

The general trends in the retrievals of integrated precipitating liquid and integrated precipitating ice are decreasing positive biases or increasing negative biases as the maximum of the distribution of each quantity is increased. Over water surfaces, the AMPR-only retrievals of integrated precipitating liquid show a total negative bias of only 4% (see Fig. 8a). EDOP-only retrievals are biased to a greater degree: the magnitude of the negative bias in integrated precipitating liquid retrievals increases to a maximum of 10% over the entire database. Similar trends are seen in the retrievals of integrated precipitating ice (Fig. 8b). AMPR-only and EDOP-only retrievals of integrated precipitating ice have total negative biases of 7% and 8%, respectively. The bias in the EDOP-only retrievals of integrated precipitating liquid is only slightly altered by combining the EDOP with the AMPR data. Figure 8a suggests, however, that the bias in the AMPR + EDOP integrated precipitating liquid retrievals might be further reduced if greater relative weight (or equivalently, a smaller error standard deviation) is assigned to the AMPR observations, since the negative bias in the AMPR-only retrievals is less than half of the bias in the EDOP-only retrievals.

Over land, AMPR-only retrievals of integrated liquid precipitation exhibit significant biases over a range of water contents due to the ambiguity between liquid precipitation emission and emission from the land surface backgrounds (Fig. 9a). EDOP-only retrievals, which are unaffected by the surface type, show an increasing negative bias with increasing integrated precipitating liquid amount that is identical to the trend seen in the

overwater retrievals. The biases in combined AMPR + EDOP retrievals of precipitating liquid are also very similar to those over water. AMPR-only, EDOP-only, and AMPR + EDOP retrievals of precipitating ice over land backgrounds show nearly the same negative bias trends as those over water (Fig. 9b). However, due to the limited scattering signal from precipitating ice amounts less than 1 kg m^{-2} , the magnitudes of biases are greater in AMPR-only retrievals for small ice amounts.

The biases in retrieved surface rain rates, although not shown, closely follow the trends seen in the integrated precipitating liquid retrievals.

Since the supporting cloud/radiative model database and synthetic observations are bias free, the biases reported in this section are inherent to the retrieval method itself. The trends in the retrieval biases can be explained with the aid of Figs. 4 and 5, which illustrate the "single-channel" retrieval of integrated precipitating liquid over water from 10.7-GHz brightness temperatures and mean radar reflectivities, respectively. Note that as the 10.7-GHz brightness temperatures and radar reflectivities in the supporting database increase, the integrated precipitating liquid amounts increase, but in addition the variance of precipitation amounts associated with a given brightness temperature/radar reflectivity also increases. It was previously shown that a greater variance of precipitation amounts for a given brightness temperature/radar reflectivity in the supporting database leads to greater random error in a precipitation estimate if that brightness temperature/radar reflectivity is observed. The potential for bias of either sign in the retrieved precipitation amount also increases, because in the absence of specific information from the brightness temperature/radar reflectivity observation, the retrieved precipitation amount from Eq. (17) reverts to the mean of the precipitation distribution corresponding to that observation in the supporting database. If the mean of the precipitation distribution in the supporting database is lower (higher) than the mean of the observed precipitation distribution, then a negative (positive) bias will result.

The bias trends seen in the multichannel synthetic retrievals are analogous to the biases seen in the single-channel retrievals of Figs. 4 and 5. Although the synthetic data from time 210 of the TOGA COARE simulation have a distribution similar to that of the supporting cloud/radiative model data (Fig. 4a), it is evident from Fig. 4b that for a given 10.7-GHz brightness temperature, the mean values of integrated precipitating liquid in the synthetic database (long-dashed curve) are greater than those of the supporting database (solid curve) for precipitating liquid amounts greater than 10 kg m^{-2} . Since retrievals using Eq. (17) are based solely on the supporting data, retrievals at these high precipitating liquid amounts should be, on average, low biased if only the 10.7-GHz brightness temperature data are utilized. Not surprisingly, low biases

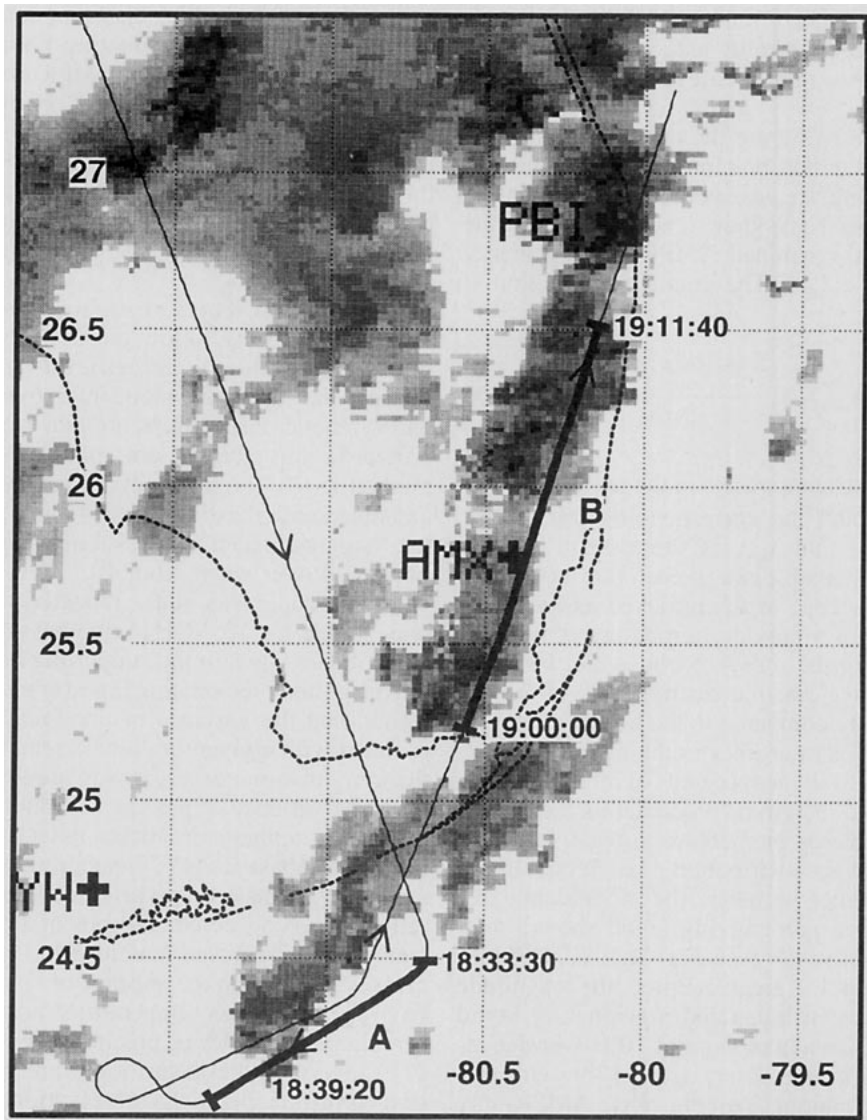


FIG. 10. Map of the ER-2 aircraft flight track on 5 October 1993 during the CAMEX experiment. Arrows indicate the flight direction, and noted times are in UTC. The flight track is superimposed on a map of the Florida peninsula, with a composite of echoes (shading) from the WSR-88D radar at 1900 UTC. AMPR and EDOP data from enhanced flight segments over water (segment A) and over land (segment B) are used in cloud/precipitation profile retrievals.

are also seen in the AMPR-only synthetic retrievals of precipitating liquid amounts greater than 10 kg m^{-2} (Fig. 8a). A persistent and increasing negative bias in the supporting data with respect to the synthetic data is evident in the single-channel EDOP retrieval plot of Fig. 5b (again, compare the long-dashed to the solid curve in the figure). Again, the same bias trend is seen in EDOP-only synthetic retrievals (Fig. 8a).

It should be emphasized that the biases of the retrieved precipitation estimates result from observations that are nonspecific. If a set of brightness temperatures/radar reflectivities always corresponded to a unique precipitation amount, then no bias would result. The

only way to correct for these inherent biases within the framework of the current retrieval method is to include additional channels or other information that can be used to better discriminate between the higher integrated precipitating liquid/ice amounts.

c. Retrievals from CAMEX

During September and October 1993, a miniexperiment called the Convection and Atmospheric Moisture Experiment (CAMEX) was conducted at the NASA Wallops Flight Facility. During CAMEX the NASA ER-2 aircraft was instrumented with microwave and

visible–infrared sensors, including the AMPR and the EDOP.

The flight track of the NASA ER-2 aircraft on 5 October 1993 is shown in Fig. 10, relative to a composite of National Weather Service WSR-88D radar data from Florida at 1900 UTC. Between 1833:30 and 1839:20 UTC, coincident nadir-looking AMPR and EDOP observations were collected with the ER-2 flying at an altitude of 20 km above a convective system over the Florida Straits (flight segment A). Later, between 1900:00 and 1911:40 UTC, AMPR and EDOP data were collected during an ER-2 overflight of a line of thunderstorms along the eastern coast of Florida (flight segment B).

Due to a time offset in the AMPR and EDOP data clocks, nadir observations from the two instruments are spatially coregistered by examining lags between the aircraft altitude and attitude parameters (logged with the AMPR data), and the range of the EDOP surface gate measured during banking maneuvers both before and after the described flight segments. Also, the EDOP observations from both flight segments are time-integrated over consecutive 3-s intervals to synchronize with the 3-s scan period of the AMPR. At a nominal ER-2 airspeed of 200 m s^{-1} , the (3 s) horizontal sample spacing is 600 m.

The traces of AMPR brightness temperatures and EDOP reflectivities recorded during flight segment A are presented in Figs. 11a and 11b, respectively, as the ER-2 traversed the convective system from the northeast to the southwest, in a direction opposite to the low-level wind shear. The 1200 UTC sounding on the same day from Key West may be seen in Figs. 2a and 2b of Heymsfield et al. (1996). Relative to the ambient wind shear, the system exhibits a convective leading edge at the 60-km mark, with reflectivities exceeding 45 dBZ from the surface up to 4 km. Downshear (to the left) of the leading edge appear to be decaying convective cells near the 48-km mark, as well as light stratiform “anvil” precipitation aloft with reflectivities between 20 and 30 dBZ. Also, there is an obvious downshear tilt in the EDOP-observed convective cells.

The precipitation structures observed by the radar are reflected in the brightness temperature traces of Fig. 11a. For example, at 10.7-GHz the brightness temperature increases from the background ocean surface value of 140 K to a maximum of 250 K associated with liquid precipitation emission from the convective leading edge. The trailing convective cells produce smaller but significant peaks in brightness temperature. Clear-air/ocean background emission increases with channel frequency, as seen in the 19.35- and 37.1-GHz data, but greater emission from precipitating liquid is still evident in rain regions, reaching saturation at roughly 270 K in the broad convective zone between 40 and 60 km. In contrast, water vapor and cloud emission saturate the 85.5-GHz channel observations even outside of the rain areas, but microwave scattering by precip-

itation-sized ice particles can depress the observed brightness temperatures significantly. Most prominent are the brightness temperature depressions at 58 and 38 km, which are associated with peak radar reflectivities greater than 30 dBZ at altitudes up to 8 km. Since the freezing level is located at 4.7 km, it may be inferred that the scattering depressions at 85.5 GHz and peak radar reflectivities aloft are associated with precipitation-sized ice.

The retrieval method is applied to the AMPR data, and then to the combined AMPR and EDOP data, assuming observation and simulation error standard deviations of $\sigma_o = \sigma_s = 2\sigma_n$ for both the AMPR and EDOP. To provide an initial consistency check, *retrievals* of the precipitation-equivalent 9.72-GHz radar reflectivity structures derived from the AMPR and AMPR+EDOP data and Eq. (17) are presented in Figs. 11c and 11d, respectively. The vertical cross section of reflectivities retrieved using the AMPR data alone exhibits many of the features of the observed EDOP reflectivities; however, the maximum low-level reflectivities and high-resolution vertical structure of the EDOP observations are not reproduced. Retrieval of the low-level maxima and high-resolution vertical reflectivity structure are only possible using the AMPR data in combination with the EDOP data in the retrieval method, as seen in Fig. 11d. Plots of the root-mean-square deviations between the retrieved and observed radar reflectivity profiles are shown in Fig. 11e. Compared to the AMPR-only retrievals, the profiles retrieved using the combined AMPR and EDOP observations are a better fit to the observed reflectivity profiles. The rms deviation of the AMPR+EDOP retrieved reflectivities over the entire flight segment is 2.71 dBZ, which is comparable to the absolute error of the EDOP reflectivity observations, estimated to be within ± 3 dBZ by Caylor et al. (1994).

However, Figs. 11d and 11e indicate some discrepancies between the retrieved and observed reflectivity profiles that are significantly greater than those that may be explained by errors in the observations or model-computed reflectivities. These discrepancies are apparent in the vicinity of the system’s convective leading edge, where the retrieved reflectivity contours lack the detail seen in the observations, and the rms reflectivity deviations of individual profiles sometimes exceed 4 dBZ. These discrepancies may be partly attributed to the loss of sensitivity in both the radiometer and radar measurements for large precipitation water contents, which contributes to greater ambiguity in the retrieved precipitation profiles associated with convective precipitating clouds. Also, although a large number of convective cloud profiles are present in the supporting cloud/radiative model database, some less commonly observed profiles may not be adequately represented. Future efforts should focus on the creation of an extended profile database drawn from precipitating clouds simulated for a variety of realistic environments.

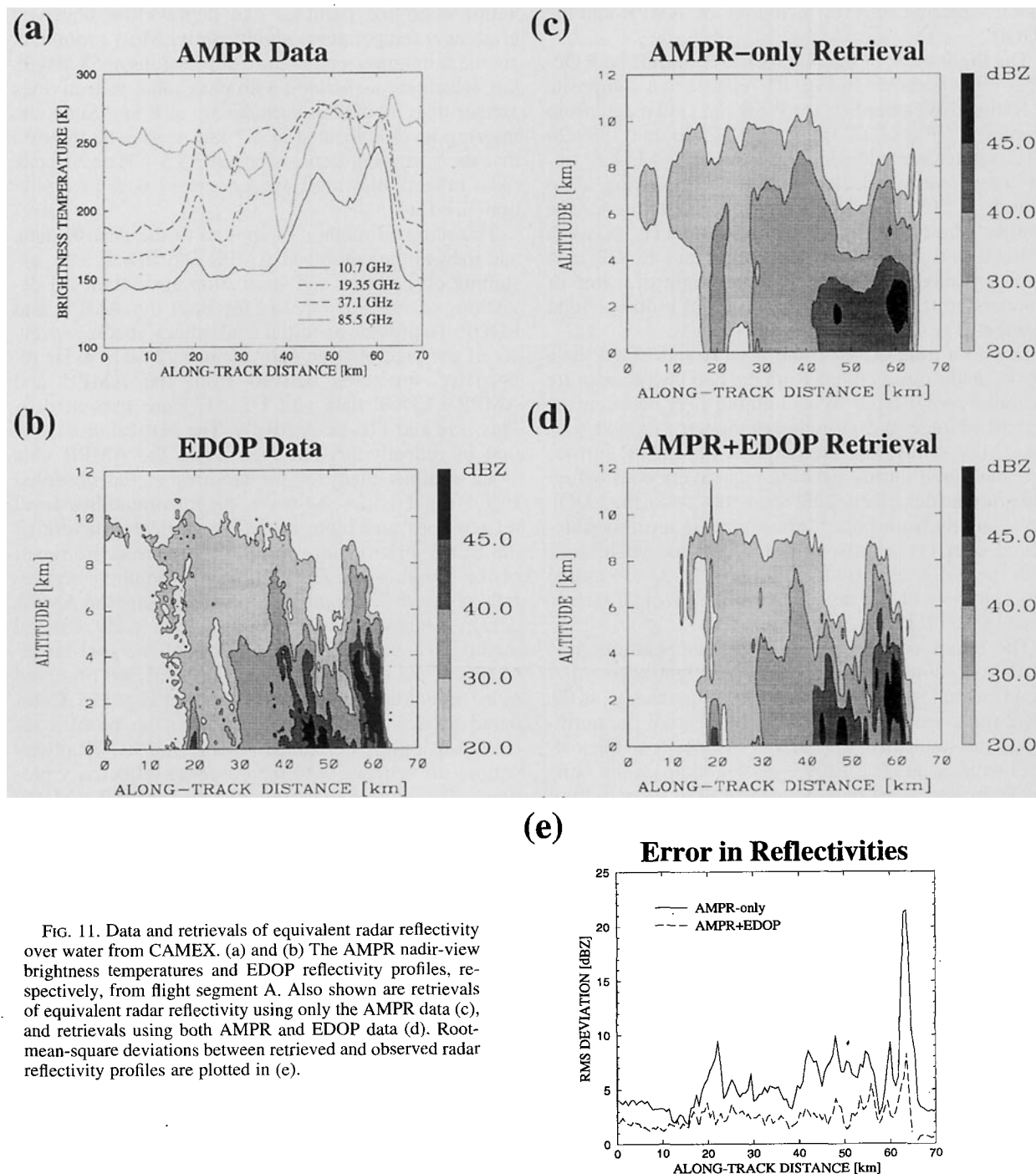


FIG. 11. Data and retrievals of equivalent radar reflectivity over water from CAMEX. (a) and (b) The AMPR nadir-view brightness temperatures and EDOP reflectivity profiles, respectively, from flight segment A. Also shown are retrievals of equivalent radar reflectivity using only the AMPR data (c), and retrievals using both AMPR and EDOP data (d). Root-mean-square deviations between retrieved and observed radar reflectivity profiles are plotted in (e).

Observations and reflectivity retrievals from flight segment B are presented in Figs. 12a–d. In this segment the ER-2 traversed a line of thunderstorms along the southeastern coast of Florida. Although both convective and stratiform rain regions are evident in the EDOP reflectivity observations (Fig. 12b), the precipitation signal in the AMPR brightness temperatures (Fig. 12a) is relatively weak. There are two reasons for

the lack of signal: first, since flight segment B is over land, upwelling brightness temperatures from the highly emissive land surface, which are about 270 K, are indistinguishable from the emission from precipitation in the emission-dominated 10.7-, 19.35-, and 37.1-GHz channels. Also, the scattering signal at 85.5 GHz associated with convective precipitation is subdued, since the observed convection is too weak to pro-

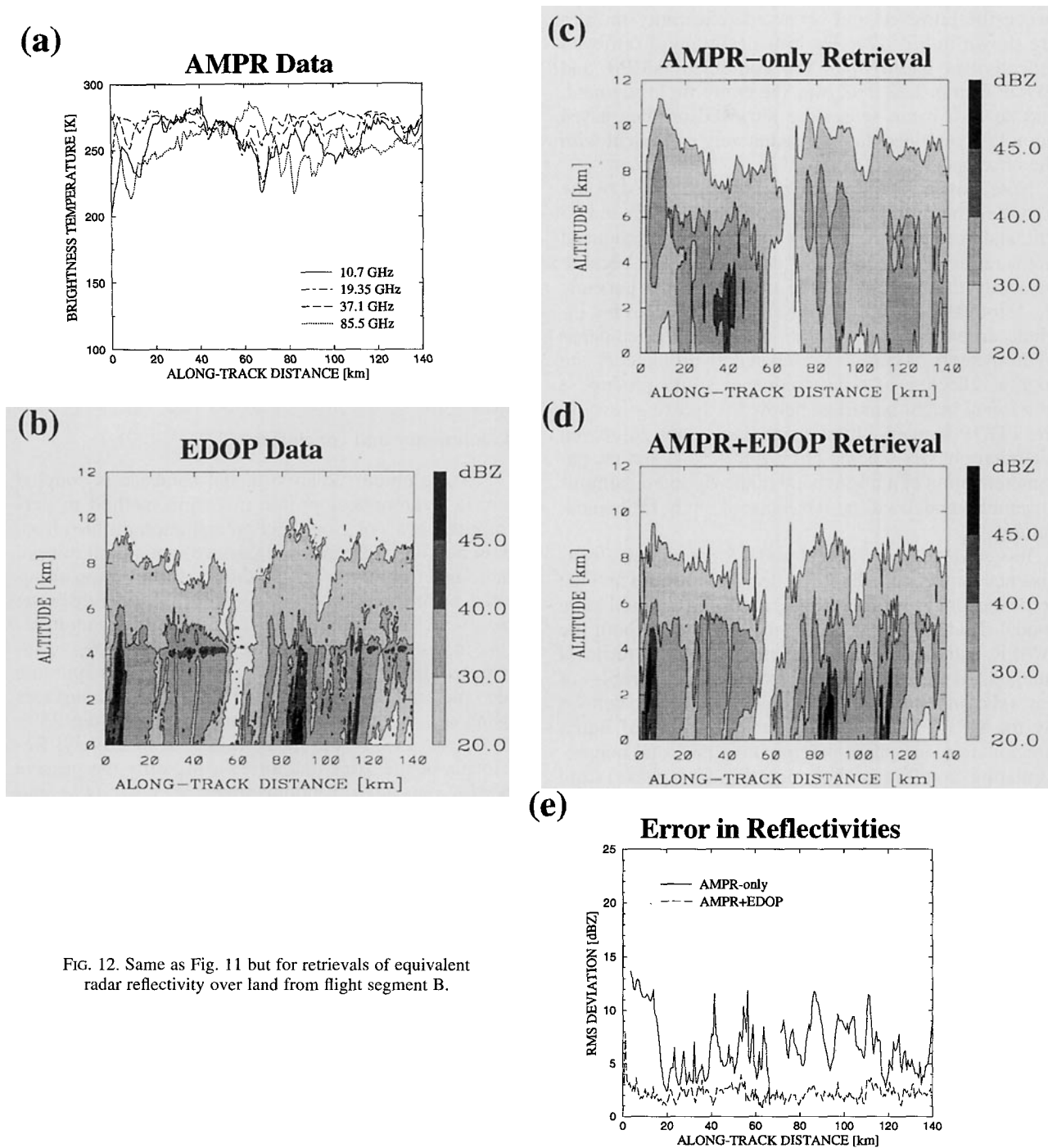


FIG. 12. Same as Fig. 11 but for retrievals of equivalent radar reflectivity over land from flight segment B.

duce large amounts of precipitation-sized ice. Note that in this case the 30-dBZ contours from cells at the 5- and 87-km marks barely exceed 6 km in altitude. Although present, the scattering depressions associated with these cells do not fall below 215 K.

As a consequence of the relatively weak precipitation signal in the AMPR observations, the AMPR-only retrievals of precipitation structure shown in Fig. 12c

are largely erroneous. In situations where little signal is present, the retrieval method simply yields the mean of the many model profiles that are radiatively consistent with the observations. As seen in Fig. 12d, the EDOP data provide the precipitation signal that is lacking in the passive radiometer data over land, and the retrieved reflectivity cross section is quite similar to the observed reflectivity structure. The rms deviations be-

tween the retrieved and observed reflectivity profiles are shown in Fig. 12e. The rms deviation of retrieved reflectivities based upon the combined AMPR and EDOP data is 2.32 dBZ over the entire flight segment, and so in a mean sense, the retrieved profiles based upon the combined data are radiatively consistent with the observations.

Note, however, that the bright bands observed by the EDOP in the stratiform rain regions between 25 and 55 km, and between 120 and 140 km, are not reproduced in the retrieval. The bright bands do not appear because presently the cloud/radiative model used to generate the retrieval method's supporting database does not include an explicit representation of melting ice-phase hydrometeors. These water-coated hydrometeors are highly reflective at radar frequencies and produce a horizontal bright band just below the freezing level in the EDOP imagery. Implementation of the improved ice microphysics scheme of Ferrier (1994) and the parameterization of a bright band in the Goddard cumulus ensemble model will be the focus of study in the near future.

It is evident from Figs. 11 and 12 that radiative consistency between the EDOP reflectivity profiles and the retrieved profiles from the supporting cloud/radiative model database can generally be achieved if both the AMPR and EDOP data are utilized in the retrieval method. Associated with each profile are the profiles of several cloud/precipitation species that are also defined by the GCE model. Vertical cross sections of liquid precipitation, ice-phase precipitation, and total nonprecipitating cloud water (both liquid and ice-phase) from the combined AMPR + EDOP retrievals are shown in Figs. 13a–c (CAMEX A) and Figs. 13d–f (CAMEX B), respectively.

Since the retrieved water content profiles of Fig. 13 are cloud model based, it is not surprising that these profiles are generally consistent with our basic understanding of convective system structure. Embedded convective cells, such as those near the 48- and 60-km marks of segment A and at 5, 85, and 112 km of segment B are associated with relatively high liquid and ice-phase precipitation water contents. Water contents of precipitating liquid in the convective cells usually exceed 1.0 g m^{-3} , and extend from the surface up to the freezing level. These convective cells extend above the freezing level at least 1 or 2 km, with water contents greater than 1.0 g m^{-3} in the form of precipitating ice. Stratiform rain regions are characterized by horizontally uniform distributions of liquid and ice precipitation with lower water contents. Precipitation water contents in the stratiform regions do not exceed 0.5 g m^{-3} in either flight segment. The retrieved precipitation distributions are compatible with limited radar climatologies of convective and stratiform precipitation in the Tropics (e.g., Leary and Houze 1979a,b; Szoke et al. 1986; Szoke and Zipser 1986).

Of particular interest are the retrieved distributions of nonprecipitating liquid and ice-phase cloud water shown in Figs. 12c and 12f. Typically, the signal from nonprecipitating cloud in passive or active microwave radiometer measurements is not distinguishable from that of precipitation. However, since the retrieval method described in this study is cloud model based, profiles of nonprecipitating cloud may be retrieved due to their correlation with the water contents and vertical structures of precipitation, which have stronger radiative signals in the remotely sensed data. Most of the significant cloud water contents retrieved from the CAMEX flight segment data are associated with regions of convection, an association documented in both cloud modeling studies (Adler et al. 1991), and observational studies (e.g., Jorgensen, 1984).

4. Summary and conclusions

A large cloud/radiative model database is coupled with a hydrometeor profile inversion method to perform retrievals of cloud and precipitation profiles from both passive and combined passive–active microwave radiometer systems. The method is tested using simulated nadir-view observations from the aircraft-borne passive AMPR and active EDOP sensors. Random errors in instantaneous, 1-km resolution estimates of integrated precipitating liquid, integrated precipitating ice, and surface rain rate over water or land surfaces using the combined AMPR and EDOP data are 23%, 19%, and 53% of the mean values, respectively. Retrievals of the same quantities using only the passive AMPR data yield random errors of 37%, 34%, and 53% over water surfaces, and 66%, 35%, and 88% over land surfaces. The magnitudes of biases in the AMPR + EDOP retrieved precipitation amounts over water or land surfaces are 8%, 9%, and 9% for integrated precipitating liquid, integrated precipitating ice, and surface rain rate, respectively.

The bias in retrieved precipitation amounts is shown to be linked to the difference in the mean precipitation amounts of the retrieval method's supporting cloud/radiative model database relative to the observed precipitation amounts. However, the biases in AMPR-only retrievals of integrated precipitating liquid and surface rain rate over water surfaces (4% and 6%, respectively) are substantially less than the biases in EDOP-only retrievals of the same quantities (10% and 13%). This result suggests that AMPR-based estimates of liquid precipitation amounts using the described retrieval method may be less sensitive to systematic differences in the supporting database than the EDOP-based estimates. Preliminary testing by the authors indicates a greater weighting of the AMPR channels can help to further reduce the EDOP liquid precipitation retrieval bias in combined AMPR + EDOP retrieval applications, but at the expense of greater random errors. More study will be required to confirm these results.

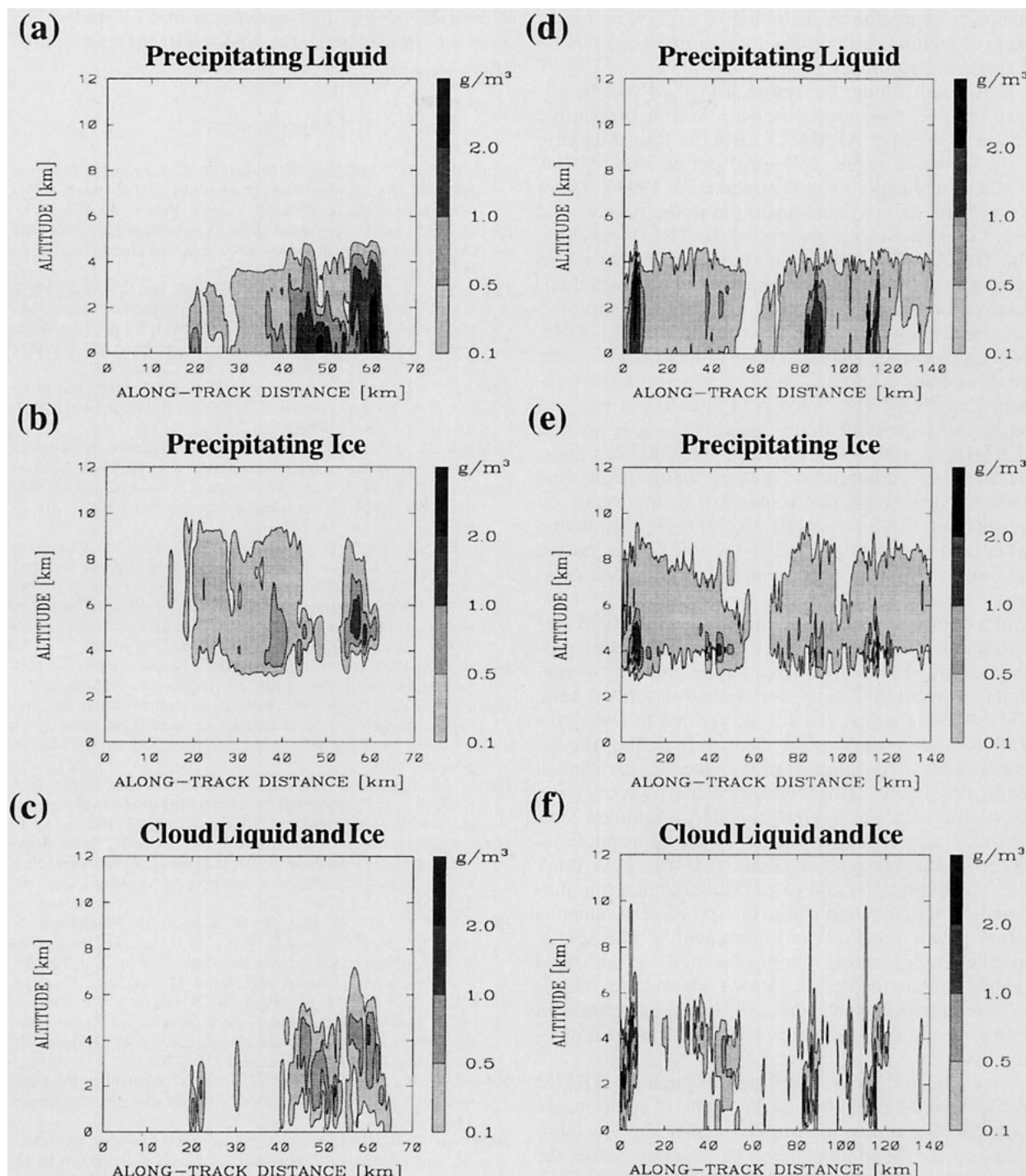


FIG. 13. Retrieved cloud and precipitation water content profiles from CAMEX. Retrievals of precipitating liquid water content, precipitating ice water content, and total nonprecipitating cloud (liquid and ice) over water from CAMEX flight segment A are shown in panels (a), (b), and (c), respectively. The same quantities retrieved over land using data from CAMEX flight segment B are shown in panels (d)–(f).

Application of the retrieval method to combined-AMPR and EDOP observations of storms from CAMEX yields retrieved cloud and precipitation vertical profiles that are consistent with basic descriptions

of tropical convective system structure. Most notably absent from retrievals is the radar “bright band,” which is observed just below the freezing level in stratiform precipitation regions; however, this problem

should be overcome by including an explicit representation of melting, water-coated ice hydrometeors in the cloud/radiative model.

In the near future, the retrieval method will be applied to nearly coincident observations from the passive AMPR and active ARMAR (Airborne Rain Mapping Radar), which were collected during the TOGA COARE field experiment (Durden et al. 1994). These instruments serve as analogs to the future passive and active microwave components of the TRMM satellite. The TRMM will be fitted with the TRMM Microwave Imager, a conically scanning passive sensor with dual-polarization channels at 10.65, 19.35, 37.0, and 85.5 GHz, and a single-polarization channel at 21.3 GHz. Both the ARMAR and the TRMM Precipitation Radar are cross-track scanning active microwave sensors operating at 13.8 GHz. Since path attenuation per unit length due to precipitation is roughly twice as great at 13.8 GHz as it is at 9.72 GHz, the unambiguous interpretation of reflectivity measurements from the ARMAR or Precipitation Radar will be more difficult in situations where vertically integrated precipitation water contents are high, and so the role of the passive radiometer channels in removing these ambiguities will be enhanced.

In a companion paper, Kummerow et al. (1996) investigate the impact of lower-resolution, satellite passive microwave measurements on the accuracy of precipitation retrievals using the method described here. The retrieval method can still be applied to lower-resolution satellite microwave data by including the effects of sensor spatial resolution in the cloud/radiative model simulations. This is accomplished by convolving the high-resolution, model-generated brightness temperature/radar reflectivity fields by the appropriate radiometer antenna patterns/radar two-way gain functions using Eqs. (7) and (8). The horizontal inhomogeneity of precipitation within the spread of the antenna patterns/gain functions is represented by the spatial distributions of precipitation generated by the cloud model. The simulation of TRMM Microwave Imager and Precipitation Radar data, including the effects of sensor resolution, is described in Olson and Kummerow (1996).

Synthetic retrievals based upon simulated TRMM data will be the focus of a future study. In addition, the retrieval of total heating profiles, which are also simulated by the cloud model, will be attempted using the same retrieval method framework. Since the retrieval method described herein is computationally efficient, it is hoped that the method can be applied operationally to TRMM microwave sensor measurements to provide precipitation and latent heating profile information.

Acknowledgments. The authors wish to thank Jeff Caylor, Wei-Kuo Tao, Brad Ferrier, Steve Lang, Yansen Wang, J. Marshall Shepherd, Bob Meneghini, Toshio Iguchi, Jack Schols, James Shiue, Dave Short, and

Robbie Hood for their assistance in this study. The work was funded under the NASA TRMM science program.

REFERENCES

- Adler, R. F., H.-Y. M. Yeh, N. Prasad, W.-K. Tao, and J. Simpson, 1991: Microwave simulations of a tropical rainfall system with a three-dimensional cloud model. *J. Appl. Meteor.*, **30**, 924–953.
- Barnes, G. M., and K. Sieckman, 1984: The environment of fast- and slow-moving tropical mesoscale convective cloud lines. *Mon. Wea. Rev.*, **112**, 1782–1794.
- Caylor, I. J., G. M. Heymsfield, S. W. Bidwell, and S. Ameen, 1994: NASA ER-2 Doppler Radar reflectivity calibration for the CAMEX project. NASA Tech. Memo. 104611, 15 pp. [Available from NASA Center for Aerospace Information, 800 Elkridge Landing Road, Linthicum Heights, MD 21090-2934.]
- Churchill, D. D., and R. A. Houze Jr., 1984: Development and structure of winter monsoon cloud clusters on 10 December 1978. *J. Atmos. Sci.*, **41**, 933–960.
- DeMaria, M., 1985: Linear response of a stratified tropical atmosphere to convective forcing. *J. Atmos. Sci.*, **42**, 1944–1959.
- Durden, S. L., E. Im, F. K. Li, W. Ricketts, A. Tanner, and W. Wilson, 1994: ARMAR: An airborne rain-mapping radar. *J. Atmos. Oceanic Technol.*, **11**, 727–737.
- Evans, K. F., J. Turk, T. Wong, and G. L. Stephens, 1995: A Bayesian approach to microwave precipitation profile retrieval. *J. Appl. Meteor.*, **34**, 260–278.
- Eyre, J. R., 1989: Inversion of cloudy satellite sounding radiances by nonlinear optimal estimation. Part I: Theory and simulation for TOVS. *Quart. J. Roy. Meteor. Soc.*, **115**, 1001–1026.
- Ferrier, B. S., 1994: A double-moment multiple-phase four-class bulk ice scheme. Part I: Description. *J. Atmos. Sci.*, **51**, 249–280.
- Haddad, Z. S., and E. Im, 1993: Optimal estimation of rain rate profiles from radar returns at attenuating wavelengths. *Proc. 26th Int. Conf. on Radar Meteorology*, Norman, OK, Amer. Meteor. Soc., 699–701.
- Hai, L., M. Xin, and C. Wei, 1985: Ground based remote sensing of LWC in cloud and rainfall by a combined dual wavelength radar–radiometer system. *Adv. Atmos. Sci.*, **2**, 93–103.
- Hartmann, D. L., H. H. Hendon, and R. A. Houze Jr., 1984: Some implications of the mesoscale circulations in tropical cloud clusters of large-scale dynamics and climate. *J. Atmos. Sci.*, **41**, 113–121.
- Heymsfield, G. M., W. Boncyk, S. Bidwell, D. Vandemark, S. Ameen, S. Nicholson, and L. Miller, 1993: Status of the NASA/EDOP airborne radar system. Preprints, *26th Int. Conf. on Radar Meteorology*, Norman, OK, Amer. Meteor. Soc., 374–375.
- , I. J. Caylor, J. M. Shepherd, W. S. Olson, S. W. Bidwell, W. C. Boncyk, and S. Ameen, 1996: Structure of Florida thunderstorms using high-altitude aircraft radiometer and radar observations. *J. Appl. Meteor.*, **35**, 1736–1762.
- Hitschfield, W., and J. Bordan, 1954: Errors inherent in the radar measurement of rainfall at attenuating wavelengths. *J. Meteor.*, **11**, 58–67.
- Jorgensen, D. P., 1984: Mesoscale and convective-scale characteristics of mature hurricanes. Part I: General observations by research aircraft. *J. Atmos. Sci.*, **41**, 1268–1285.
- , T. J. Matejka, D. Johnson, and M. A. LeMone, 1994: A TOGA/COARE squall line seen by multiple airborne Doppler radars. *Proc. Sixth Conf. on Mesoscale Processes*, Portland, OR, Amer. Meteor. Soc., 25–28.
- , —, and —, 1995: Structure and momentum fluxes within a TOGA/COARE squall line system observed by airborne Doppler radar. *Proc. 21st Conf. on Hurricanes and Tropical Meteorology*, Miami, FL, Amer. Meteor. Soc., 579–581.
- Kedem, B., H. Pavlopoulos, X. Guan, and D. A. Short, 1994: A probability distribution model for rain rate. *J. Appl. Meteor.*, **33**, 1486–1493.

- Kozu, T., K. Nakamura, R. Meneghini, and W. C. Bonczyk, 1991: Dual-parameter radar rainfall measurement from space: A test result from an aircraft experiment. *IEEE Trans. Geosci. Remote Sens.*, **29**, 690–703.
- Kumagai, H., R. Meneghini, and J. R. Wang, 1993: Combined analysis of airborne single-frequency radar and multi-frequency radiometer observations in the TRMM-1 experiment. *Proc. 26th Int. Conf. on Radar Meteorology*, Norman, OK, Amer. Meteor. Soc., 696–698.
- Kummerow, C., and L. Giglio, 1994: A passive microwave technique for estimating rainfall and vertical structure information from space. Part I: Algorithm description. *J. Appl. Meteor.*, **33**, 3–18.
- , R. A. Mack, and I. M. Hakkarinen, 1989: A self-consistency approach to improve microwave rainfall estimates from space. *J. Appl. Meteor.*, **28**, 869–884.
- , W. S. Olson, and L. Giglio, 1996: A simplified scheme for obtaining precipitation and vertical hydrometeor profiles from passive microwave sensors. *IEEE Trans. Geosci. Remote Sens.*, in press.
- Lau, K.-M., and L. Peng, 1987: Origin of the low-frequency (intra-seasonal) oscillation in the tropical atmosphere. *J. Atmos. Sci.*, **44**, 950–972.
- Leary, C. A., and R. A. Houze Jr., 1979a: The structure and evolution of convection in a tropical cloud cluster. *J. Atmos. Sci.*, **36**, 437–457.
- , and —, 1979b: Melting and evaporation of hydrometeors in precipitation from the anvil clouds of deep tropical convection. *J. Atmos. Sci.*, **36**, 669–679.
- Liebe, H. J., 1985: An updated model for millimeter wave propagation in moist air. *Radio Sci.*, **20**, 1069–1089.
- Lin, Y.-L., R. D. Farley, and H. D. Orville, 1983: Bulk parameterization of the snow field in a cloud model. *J. Climate Appl. Meteor.*, **22**, 1065–1092.
- Lorenc, A. C., 1986: Analysis methods for numerical weather prediction. *Quart. J. Roy. Meteor. Soc.*, **112**, 1177–1194.
- Marshall, J. S., and W. M. Palmer, 1948: The distribution of raindrops with size. *J. Meteor.*, **5**, 165–166.
- Marzoug, M., and P. Amayenc, 1991: Improved range-profiling algorithm of rainfall rate from a spaceborne radar with path-integrated attenuation constraint. *IEEE Trans. Geosci. Remote Sens.*, **29**, 584–592.
- Meneghini, R., 1978: Rain-rate estimates for an attenuating radar. *Radio Sci.*, **13**, 459–470.
- , and K. Nakamura, 1990: Range profiling of the rain rate by an airborne weather radar. *Remote Sens. Environ.*, **31**, 193–209.
- , J. Eckerman, and D. Atlas, 1983: Determination of rain rate from a space-borne radar using measurements of total attenuation. *IEEE Trans. Geosci. Remote Sens.*, **21**, 34–43.
- , J. R. Wang, H. Kumagai, and T. Iguchi, 1994: Description of a radar/radiometer method and its application to airborne measurements over stratiform rain. *Proc. IGARSS-94*, Pasadena, CA, IEEE Geoscience and Remote Sensing Society, 1773–1775.
- Mugnai, A., E. A. Smith, and G. J. Tripoli, 1993: Foundations for physical-statistical precipitation retrieval from passive microwave satellite measurements. Part II: Emission source and generalized weighting function properties of a time dependent cloud-radiation model. *J. Appl. Meteor.*, **32**, 17–39.
- Ogura, Y., Y.-L. Chen, J. Russell, and S.-T. Soong, 1979: On the formation of organized convection in the eastern Atlantic. *Mon. Wea. Rev.*, **107**, 426–441.
- Olson, W. S., 1989: Physical retrieval of rainfall rates over the ocean by multispectral microwave radiometry: Application to tropical cyclones. *J. Geophys. Res.*, **94**, 2267–2280.
- , and C. D. Kummerow, 1996: Simulated retrieval of precipitation profiles from TRMM Microwave Imager and Precipitation Radar data. *Proc. Eighth Conf. on Satellite Meteorology and Oceanography*, Atlanta, GA, 248–251.
- Papoulis, A., 1965: *Probability, Random Variables, and Stochastic Processes*. McGraw-Hill, 583 pp.
- Rutledge, S. A., and P. V. Hobbs, 1984: The mesoscale and microscale structure and organization of clouds and precipitation in midlatitude clouds. Part XII: A diagnostic modeling study of precipitation development in narrow cold frontal rainbands. *J. Atmos. Sci.*, **41**, 2949–2972.
- Sauvageot, H., 1992: *Radar Meteorology*. Artech, 366 pp.
- Simpson, J., R. F. Adler, and G. R. North, 1988: A proposed Tropical Rainfall Measuring Mission (TRMM) satellite. *Bull. Amer. Meteor. Soc.*, **69**, 278–295.
- Smith, E. A., X. Xiang, A. Mugnai, and G. J. Tripoli, 1994a: Design of an inversion-based precipitation profile retrieval algorithm using an explicit cloud model for initial guess microphysics. *Meteor. Atmos. Phys.*, **54**, 53–78.
- , —, —, R. E. Hood, and R. W. Spencer, 1994b: Behavior of an inversion-based precipitation retrieval algorithm with high-resolution AMPR measurements including a low-frequency 10.7-GHz channel. *J. Atmos. Oceanic Technol.*, **11**, 858–873.
- Smolarkiewicz, P. K., 1983: A simple positive definite advection scheme with small implicit diffusion. *Mon. Wea. Rev.*, **111**, 479–486.
- , 1984: A fully multidimensional positive definite advection transport algorithm with small implicit diffusion. *J. Comput. Phys.*, **54**, 325–362.
- , and W. W. Grabowski, 1990: The multidimensional positive definite transport algorithm: Nonoscillatory option. *J. Comput. Phys.*, **86**, 355–375.
- Spencer, R. W., R. E. Hood, F. J. LaFontaine, E. A. Smith, R. Platt, J. Galliano, V. L. Griffen, and E. Lobl, 1994: High-resolution imaging of rain systems with the Advanced Microwave Precipitation Radiometer. *J. Atmos. Oceanic Technol.*, **11**, 849–857.
- Szoke, E. J., and E. J. Zipser, 1986: A radar study of convective cells in mesoscale systems in GATE. Part II: Life cycles of convective cells. *J. Atmos. Sci.*, **43**, 199–218.
- , —, and D. P. Jorgensen, 1986: A radar study of convective cells in mesoscale systems in GATE. Part I: Vertical profile statistics and comparison with hurricanes. *J. Atmos. Sci.*, **43**, 182–197.
- Tao, W.-K., and S.-T. Soong, 1986: A study of the response of deep tropical clouds to mesoscale processes: Three-dimensional numerical experiments. *J. Atmos. Sci.*, **43**, 2653–2676.
- , and J. Simpson, 1989: Modeling study of a tropical squall-type convective line. *J. Atmos. Sci.*, **46**, 177–202.
- , and —, 1993: Goddard Cumulus Ensemble model. Part I: Model description. *Terr. Atmos. Oceanic Sci.*, **4**, 35–72.
- , S. Lang, J. Simpson, and R. Adler, 1993: Retrieval algorithms for estimating the vertical profiles of latent heat release: Their applications for TRMM. *J. Meteor. Soc. Japan*, **71**, 685–700.
- Trenberth, K. E., G. W. Branstator, and P. A. Arkin, 1988: Origins of the 1988 North American drought. *Science*, **242**, 1640–1645.
- Trier, S. B., D. B. Parsons, and M. A. LeMone, 1994: A three-dimensional numerical simulation of a tropical squall line observed during TOGA-COARE. *Proc. Sixth Conf. on Mesoscale Processes*, Portland, OR, Amer. Meteor. Soc., 45–48.
- Turk, J., J. Vivekanandan, F. S. Marzano, R. E. Hood, R. W. Spencer, and F. J. LaFontaine, 1994: Active and passive microwave remote sensing of precipitating storms during CaPE. Part I: Advanced microwave precipitation radiometer and polarimetric radar measurements and models. *Meteor. Atmos. Phys.*, **54**, 3–27.
- Weinman, J. A., and R. Davies, 1978: Thermal microwave radiances from horizontally finite clouds of hydrometeors. *J. Geophys. Res.*, **83**, 3099–3107.
- , R. Meneghini, and K. Nakamura, 1990: Retrieval of precipitation profiles from airborne radar and passive radiometer measurements: Comparison with dual-frequency radar measurements. *J. Appl. Meteor.*, **29**, 981–993.
- Wilheit, T. T., 1979: A model for the microwave emissivity of the ocean's surface as a function of wind speed. *IEEE Trans. Geosci. Electron.*, **GE-17**, 244–249.